Internal Wave Reflection from Sloping Boundaries

Donald N. Slinn[1] and J. J. Riley[2]

[1] Department of Civil and Coastal Engineering
University of Florida
Gainesville, FL 32611-6590

[2] Department of Mechanical Engineering
University of Washington
Seattle, WA 98195

January 2002

Submitted to the
Journal of Fluid Mechanics

Abstract

The nonlinear dynamics of internal wave reflection from sloping boundaries are studied using numerical experiments for waves propagating in a plane normal to the slope. When the angle of wave energy propagation is close to the bottom slope, the reflection causes wave breakdown into a turbulent layer near the boundary. Simulations demonstrate that the net effects of turbulent mixing are not confined to the near boundary region: they are communicated to the interior stratified fluid by motions induced by buoyancy effects and by the wave field, resulting in progressive layering and weakening of the background density gradient. Several features of the flow response are dependent on the bottom slope. For steep slopes the flow develops into a quasi-steady turbulent bore that moves along the boundary at the phase speed of the incident waves. For shallow slopes the boundary region exhibits intermittent turbulence, where approximately every 1.3 wave periods the fluid near the boundary mixes energetically and then restratifies until the next mixing cycle. Generally, the duration of the mixing cycle is similar to the wave period, with longer cycles occuring over shallower slopes. Transition to turbulence is also a function of the bottom slope and Richardson number but occurs at Reynolds numbers of approximately 600 for steep slopes ($\simeq 30^o$) and 1800 for shallow slopes ($\simeq 5^o$), based upon the wavelength and maximum current velocity of the oncoming wave train, for Richardson numbers of approximately 100. Average dissipation Reynolds numbers ($\simeq 10$) from the turbulent experiments are consistent with predictions for transition to turbulence. The turbulent layer thickness depends on the wave amplitude, with a maximum characteristic depth of approximately one half of the vertical wavelength of the oncoming wave. Strong wall shear rates are caused by wave amplification in the turbulent layer containing approximately two orders of magnitude stronger shear than present in the oncoming waves. Energy budgets for critically reflecting waves indicate that about 35% of the oncoming wave energy goes into irreversible mixing, 55% is dissipated to heat, and approximately 10% of the wave energy is reflected from the bottom slope. An exact solution to the Navier-Stokes equations for a viscously decaying plane internal gravity wave is used to examine features of mixing. The mixing efficiency is shown to be a function of the Prandtl

number for moderate Reynolds number flows.

1 Introduction

Laboratory experiments have established that internal wave reflection from sloping boundaries can activate strong mixing in turbulent boundary regions near slopes (Cacchione and Wunsch, 1974; Ivey and Nokes, 1987; Taylor, 1993). Observations of enhanced boundary mixing in the ocean are often attributed to internal wave reflection, which may provide sufficient energy to account for a significant portion of the overall oceanic vertical mixing (Wunsch and Hendry, 1972; Gordon, 1980; Eriksen, 1982, 1985, 1997; Wolanski, 1987; Huthnance, 1989; Thorpe *et al.*, 1990; Gilbert, 1993; Toole *et al.*, 1994; White, 1994; Ledwell and Hickey, 1995; Holloway and Barnes, 1997; Petruncio *et al.* 1997). The cause may be the breaking of internal gravity waves as they reflect off the continental shelf or off other sloping boundaries near islands or seamounts. In addition, wave reflection has been suggested as the source of strong boundary-shear stresses that cause persistent sediment suspension from slopes (Cacchione and Drake, 1986).

Many dynamical properties of internal gravity waves are well understood and accurately described by linear theory, and this theory has been applied to internal wave reflection, *e.g.*, Phillips (1977), Gordon (1980), Eriksen (1985). More extensive theoretical models that include interactions between oncoming and reflected waves have been developed to explain resonant forcing, the development of nonlinearities, and topographic influences, *e.g.*, Thorpe and Haines (1987), Gilbert and Garrett (1989), Thorpe (1989, 1997). Probably the most effective conditions for boundary mixing occur when an oncoming wave reflects from a bottom slope α that nearly matches the angle of wave propagation θ. In this case linear theory suggests that a small amplitude oncoming wave may be reflected with large amplitude, thus exhibiting nonlinear behavior and possibly wave break down and turbulence. The flux of reflected energy from the slope is adjusted in two ways during reflection: the wave energy is transferred to shorter wavelength (higher wavenumber), and the group velocity decreases. At the critical condition, $\theta = \alpha$, linear wave theory predicts a reflected wave of infinite amplitude, infinitesimal wavelength, and zero group velocity, leading to the trapping of oncoming wave energy in the boundary region. In such a case, nonlinearities and turbulence

must come into play.

Field observations of the spectral enhancement of internal wave energy are centered about the critical frequency associated with the bottom slope. These enhancements occur over the breadth of frequency range expected from linear theory; however, amplitudes of the reflected waves are much smaller than predicted by linear theory. The differences have been attributed to frictional dissipation near the boundary and to highly nonlinear interactions.

Laboratory experiments of internal wave reflection (Cacchione and Wunsch, 1974; Cacchione and Southard, 1974) have similarly demonstrated that wave amplification is in good agreement with linear theory for cases sufficiently far from the critical angle. Near the critical angle, though, the reflected wave amplitudes are much less than those predicted by linear theory, and the boundary region is sometimes characterized by a turbulent bore surging upslope, reminiscent of a breaking surface wave on a beach. Ivey and Nokes (1989) and Taylor (1993) observe that, for critical reflection, the boundary region may exhibit steady or unsteady turbulence, depending on the bottom slope. They find the layer thickness and the mixing efficiency (the portion of wave energy converted to potential energy through turbulent mixing) are linearly related to the incident wave amplitude, A_w, up to an upper bound at which A_w exceeds about one tenth of the amplitude of an overturning wave.

Several questions remain concerning the finite amplitude behavior of internal wave reflection from sloping boundaries. How do nonlinearity and diffusion influence wave reflection near critical conditions? In what ways does the steepness of bottom slope influence the flow response? Into what form of energy is the wave energy converted when the wave has broken down? What parameters control the thickness of the turbulent layer? Are mean currents or steady circulations induced near the slope? How is the background density profile influenced away from the boundary? Is mixed fluid in the boundary region communicated to the interior stratified regions? How far from the critical frequency can a wave be and still cause a similar response to critical reflection? How strongly are currents and shear rates amplified by wave reflection? In this paper we attempt to address these questions by reporting on numerical experiments. Preliminary results have been reported in Slinn and Riley (1996),

and details of the local instabilities and vorticity dynamics present in the boundary region for a single critical reflection experiment have been reported separately (Slinn and Riley, 1997a).

Here, we report on the major results from our numerical experiments (Slinn, 1995). The advantage of these numerical studies over previous use of linear inviscid theory is the ability to include nonlinear and diffusive effects in the model; the advantage over laboratory experiments is the ability to make available detailed information on the flow field, allowing one to address the energetics and turbulence dynamics in detail, and to facilitate flow measurement and visualizations. The paper is organized into four sections. The model and problem formulation are described briefly in Section 2, results from the numerical experiments are presented in Section 3, and Section 4 contains the summary and conclusions.

2 Model Description

When an internal wave of frequency ω propagating in a uniformly stratified environment reflects from a larger-scale, sloping boundary, the wave's angle of propagation with respect to the horizontal, θ, is preserved (Phillips, 1977). The angle between the group velocity vector and the horizontal depends upon the wave frequency, ω, and the background density stratification according to the dispersion relation $\omega = N \sin\theta$, where N is the buoyancy frequency defined by $N^2 = (-g/\rho_o)(\partial\overline{\rho}/\partial z_T)$. Figure 1 shows the wave reflection process using a ray-tube diagram based upon linear theory, and illustrates the basic problem geometry. Here α is the angle that the sloping boundary makes with the horizontal, g is the direction of gravity, the x-direction is alongslope, the x_T-direction is horizontal, the z_T-direction is opposite the direction of gravity, and the z-direction is perpendicular to the sloping boundary. This reflection from a sloping boundary can lead to an increase in the energy density of the wave, as the energy in the oncoming wave is concentrated into a more narrow ray tube upon reflection.

The numerical model is described in detail in a separate paper (Slinn and Riley, 1997b). The model simulates forced, dissipative, incompressible flow within the Boussinesq approximation (Phillips, 1977), in which the governing equations are written in terms of pressure and density fluctuations with the hydrostatic balance removed. The model is periodic in x and y and bounded by a plane wall at the bottom boundary (see Figure 1). For a sloping ocean floor, the coordinate system used in the numerical simulation is rotated as shown. The background density gradient $\partial\overline{\rho}/\partial z_T$ is assumed to be constant and used to nondimensionalized the density field, *e.g.*, $\rho^* = \rho/(L\partial\overline{\rho}/\partial z_T)$, where ρ^* represents a nondimensional variable and L is a characteristic length scale. Note that the background density and pressure fields are not periodic at the lateral boundaries in x. Since the background fields have been subtracted from the governing equations, however, if the remaining perturbation density and pressure fields are initially periodic in the x-direction, they will remain so.

The nondimensionalized governing equations in a coordinate system rotated through

angle α with respect to the vertical are

$$\nabla \cdot \mathbf{u} = 0 \ , \tag{2.1}$$

$$\frac{\partial u}{\partial t} + \mathbf{u} \cdot \nabla u + Ri\, \rho \sin\alpha = -\frac{\partial p}{\partial x} + \frac{1}{Re}\nabla^2 u + F_u \ , \tag{2.2}$$

$$\frac{\partial v}{\partial t} + \mathbf{u} \cdot \nabla v = -\frac{\partial p}{\partial y} + \frac{1}{Re}\nabla^2 \ , \tag{2.3}$$

$$\frac{\partial w}{\partial t} + \mathbf{u} \cdot \nabla w + Ri\, \rho \cos\alpha = -\frac{\partial p}{\partial z} + \frac{1}{Re}\nabla^2 w + F_w \ , \tag{2.4}$$

$$\frac{\partial \rho}{\partial t} + \mathbf{u} \cdot \nabla \rho - w\cos\alpha - u\sin\alpha = \frac{1}{Pr\ Re}\nabla^2 \rho + F_\rho \ , \tag{2.5}$$

where the *'s have been dropped from the nondimensional variables for convenience throughout. The nondimensional parameters (the Richardson, Reynolds, and Prandtl numbers) are

$$Ri = \left(\frac{NL}{U}\right)^2 \ , \quad Re = \frac{UL}{\nu} \ , \quad Pr = \frac{\nu}{\kappa} \ , \tag{2.6a-c}$$

where L and U are characteristic length and velocity scales, respectively, and ν and κ are the diffusivities of momentum and density; the forcing terms are described immediately below.

During simulations, incoming waves are forced continuously from inside the computational domain, utilizing the forcing terms on the right hand sides of the governing equations. Both the velocity and density fields are locally forced in a manner that generates a monochromatic wave train with specified frequency and wavenumber vector incident upon the sloping terrain. The forcing functions in the rotated coordinate system are specified using the relations

$$F_u = -\frac{Am}{k}\, F(z) \cos(kx + mz - \omega t) - \frac{A}{k}\, F'(z) \sin(kx + mz - \omega t) \ , \tag{2.7}$$

$$F_w = AF(z) \cos(kx + mz - \omega t) \ , \tag{2.8}$$

$$F_\rho = \frac{-A\cos\alpha\, F(z)}{\omega}\, \sin(kx + mz - \omega t) + \frac{Am\sin\alpha\, F(z)}{\omega\ k} \sin(kx + mz - \omega t) - \frac{A\sin\alpha\, F'(z)}{\omega\ k}\, \cos(kx + mz - \omega t) \ . \tag{2.9}$$

Following Winters (1989), the localization function $F(z)$ is

$$F(z) = \exp[-b(z - z_0)^2], \ \ 0 \le z \le L_z \ , \tag{2.10}$$

where L_z is the height of the computational domain in z, and the forcing is centered at $z_0 = 2L_z/3$. Note that the forcing implies that the oncoming wave is in the vertical plane defined by the normal to the boundary.

No-slip boundary conditions on velocity are employed at the bottom boundary, while a zero flux boundary condition is used for the density field,

$$\frac{\partial \rho}{\partial z} = -\cos\alpha \quad \text{at} \quad z = 0 \ , \tag{2.11}$$

where the total density field, when nondimensionalized by $\partial\overline{\rho}/\partial z_T$ in the rotated coordinate system is $\rho_t = \rho_0 - z\,\cos\alpha - x\,\sin\alpha + \rho$. Above the wave forcing region is a numerical open boundary condition utilizing a Rayleigh damping sponge layer (Durran *et al.*, 1993) that absorbs outgoing wave energy with minimal reflection.

The model uses a variable grid with a higher density of computational nodes near the bottom boundary. The grid resolution for the experiments is typically of the order of 128^3 grid points. For the higher Reynolds number experiments, *e.g.,* for $Re > 2000$ (presented in the next section), the model incorporates additional artificial numerical dissipation at the smallest resolved length scales. This is accomplished by adding hyperviscosity terms, *e.g.,* $\mu\nabla^6\mathbf{u}$, $\mu\nabla^6\rho$ with $\mu \ll 1$, to the momentum and density equations to filter energy at poorly resolved scales of motion. The method incorporates the compact filtering techniques of Lele (1992) and is presented in detail in Slinn and Riley (1997b). Since internal wave reflection is not microscale driven, modeling of small-scale dissipation with a hyperviscosity does not dominate or invalidate the useful information derived from the results.

For analysis of the experiments we use the volume averaged kinetic, potential, and total energy equations. The kinetic energy is defined by $(u^2 + v^2 + w^2)/2$, the potential energy by $Ri\,\rho^2/2$ (Winters *et al.*, 1995), and the total energy is their sum. Consider the equation for the volume averaged kinetic energy, defined for a control volume extending from the sloping boundary to the base of the sponge layer:

$$\frac{\partial\,\overline{KE}}{\partial t} = \frac{1}{V}\int_V \left[B_f + \epsilon + F_{KE} + W_{KE}\right]\, dV$$
$$+\frac{1}{L_x L_y}\int_0^{L_x}\int_0^{L_y} \left[(w\cdot KE)|_{z=top} + \ (w\cdot p)|_{z=top}\right]\, dx\, dy \ . \tag{2.12}$$

Here F_{KE} is the dissipation of kinetic energy by the hyperviscosity filter, ϵ is the kinetic energy dissipation rate (Batchelor, 1967), the buoyancy flux is $B_f = Ri\,\rho\,(w\cos\alpha + u\sin\alpha)$, and the work input by the wave forcing mechanism is $W_{KE} = uF_u + wF_w$. The last two terms represent the advective and radiative fluxes, respectively, of kinetic energy through the upper boundary of the control volume.

The volume averaged potential energy equation is

$$\frac{\partial\,\overline{PE}}{\partial t} = \frac{1}{V}\int_V \left[-B_f + \chi + F_{PE} + W_{PE}\right]\,dV$$
$$+\frac{1}{L_x L_y}\int_0^{L_x}\int_0^{L_y}\,\left[(w\cdot PE)|_{z=top}\right]\,dx\,dy\ . \tag{2.13}$$

Here F_{PE} is the dissipation of potential energy by the filter, χ is the potential energy dissipation rate (Winters *et al.*, 1995), and $W_{PE} = Ri\,\rho\,F_\rho$ is the work input from the wave forcing mechanism. The last term represents the advective flux of potential energy through the upper boundary of the control volume.

Low level white noise is included as part of the initial conditions, and the internal wave forcing is started from rest at $t = 0$. After a short startup period a quasi-steady flow develops in which a beam of sinusoidal internal waves propagate toward, and interacts with, the bottom boundary.

3 Results

This section contains results from the numerical experiments. The internal wave reflection results are presented in four subsections: 1) examples of critical angle reflection, 2) properties of the turbulent layer, 3) energetics and mixing efficiencies, and 4) off-critical angle reflection. Subsection 3.2 on the properties of the turbulent layer includes description of flow properties including transition to turbulence, turbulent layer thickness, vertical diffusion rates, the magnitude of wall shear rates, and changes to the background density profiles.

Approximately fifty different high resolution three-dimensional simulations were conducted to investigate the internal wave reflection problem. Table 1 lists identifying details for critical angle experiments along with parameters for each case. The critical angle experiments were done for bottom slopes between 3.4^o and 30^o, with special focus on the 9.2^o, 20^o and 30^o slopes. The Reynolds, $Re = U\lambda/\nu$, and Richardson numbers, $Ri = (N\lambda/U)^2$, listed in Table 1 are based upon the maximum current speed and wavelength of the oncoming wave. The wave frequency ω is normalized by the buoyancy frequency N. One of the quantities of interest in these experiments is the transition point from laminar flow to wave breakdown into turbulence. The information in the "Classification" column of Table 1 is generally related to this point. Cases 16 and 17 were conducted for Prandtl numbers different from unity and Cases 25 and 26 were conducted using the same nondimensional parameters as Case 24, but with different domain sizes, doubling the domain in either the x- or y-direction. These latter cases demonstrate the independence of the results to the dimension of the across-slope domain length scale L_y or to the number of wavelengths of the oncoming wave in the x-direction. Cases 29, 32, and 33 were also conducted using two wavelengths of the oncoming waves in the x-direction, and each developed into turbulent flows.

3.1 Critical Reflection Examples

Details of a critical-angle reflection experiment are presented to introduce the basic flow features that develop. This experiment (Case 26 in Table 1) is conducted over a 20^o bot-

tom slope with $Re = 1800$ and $Ri = 92$. The wave period for these simulations is 18.4, approximately three times the buoyancy period of 2π. Figure 2 shows, through approximately one wave period, isopycnals of finite amplitude waves emerging from the region of wave forcing, approaching, and interacting with the sloping bottom boundary. The figure is a two-dimensional (x, z) cross section from a three-dimensional simulation. The figures are shown to scale, focusing on the region near the bottom slope to a height $z_T = 2\lambda_z$ (the full domain extends to $z = 4\lambda_z$). The experiment was conducted with two horizontal wavelengths of the oncoming waves in the domain. The first frame of Figure 2 shows two regions of strong density gradient, or thermal fronts (Thorpe, 1993), in the near-wall region. These features move upslope at the x-component of the phase speed of the oncoming wave and, as time progresses, develop large scale, statically unstable density inversions above and in the lee of the front. The oncoming gravity waves can be seen in the upper portion of the figures.

As time progresses, the instability breaks down and the wave energy is dissipated by small scale mixing, which reaches a peak at approximately $t = 89$. Between $t = 89$ and 97 the boundary layer restratifies and relaminarizes, decreasing the three-dimensionality of the flow. By the last frame of Figure 2, at $t = 97.6$, the flow has returned to a situation very similar to the initial frame. Additional analysis, given below, shows that the pattern repeats itself during subsequent wave periods with only minor variation. The variability may be attributed to the complexity of the nonlinear interactions of the turbulence during the subsequent (and previous) mixing cycles. Taylor (1993) studied a similar flow involving critical reflection over a 20^o bottom slope in the laboratory using a ducted, trapped, type of oncoming internal wave. With the type of wave used for the wave tank experiments the mixing results are phase locked with the wave period. This restriction is overcome in the numerical simulations, where the dynamics are free to develop at rates different from the wave period. Yet, despite the significant differences in method, many of the flow features that develop are similar.

In the simulations, the boundary region experiences a spatially periodic oncoming wave, which always includes regions of both upslope and downslope flows. Figure 3 shows two-

dimensional velocity vectors for Case 26, at the same times as Figure 2. The calculations were carried out on a higher resolution (3-D) mesh, but are presented on a coarse mesh to enhance the visibility of the larger scale features. A reference vector with magnitude $|\mathbf{u}| = 0.12$ is plotted outside the domain to indicate the velocity scales.

The location of the thermal front is indicated in the first and last frames of Figure 3 by the upwelling seen in the velocity field near the wall. Above the thermal front, there is an upslope flow across a considerable portion of the horizontal (x) domain at a height of approximately $z = 0.5\lambda_z$. The upslope phase of the flow, especially evident at $t = 75.5$ and 97.6, extends from the downward flow of the oncoming gravity wave and spreads out in the x-direction. As these upslope currents move parallel to the boundary they carry denser fluid, creating static instabilities locally. This mechanism leads to wave overturning and breakdown in the boundary region. In addition, there is a strong region of shear between upwelling fluid flowing downslope and over the thermal front and the upslope currents. The turbulent phase of the wave cycle is strongest during the two frames at $t = 82.9$ and 88.9. Throughout the mixing cycle, advection from the oncoming wave shear plays an important role in the development of the turbulent layer. During mixing, the phase of the wave with downward flow injects ambient stratified fluid into the base of the turbulent layer, while the phase of the wave with upward flow extracts fluid from the top.

During the period of boundary region relaminarization and restratification, the flow near the boundary is predominantly downslope. For example, at $t = 93$ (not shown) a strong downslope flow in the boundary region is located at approximately the distance from the wall where earlier the upslope flow had set up static instabilities.

While the oscillations of upslope and downslope flow are consistent with the observations of Taylor (1993), they arise from different mechanisms. The numerically simulated flows are not uniformly upslope or downslope across the full breadth of the boundary layer in the region $0.1\lambda_z < z < 0.3\lambda_z$. It is clear, however, that localized regions leading to the development of turbulence and wave breakdown are set up by patterns similar to those observed in the laboratory. The formation of locally unstable regions appears to be related

to a complicated nonlinear interaction between the phase of the oncoming wave and the buildup of energy (radiated waves) in the boundary region. The simulations indicate that turbulence is correlated with the development of local regions with static instabilities.

In Figure 4 the velocity field is shown in an x-y plane parallel to the sloping bottom plane at a distance from the wall of $z = 0.137\lambda_z$. The vectors appear to indicate a divergent flow because they show only the components of velocity in the x-y plane and do not include the w component. Several distinct horizontal structures are apparent in the flow. The observed variability in the y-direction indicates the importance of the three-dimensionality of the wave breakdown process. If regions of high variability of the v component are compared with the density fields of Figure 2, then the strongest three-dimensionalities are seen to occur at (and move with) the location of the thermal front.

Maximum velocities in the boundary region are shown as a function of time in Figure 5 for four critical angle experiments over the 20^o bottom slope, and are labeled by their Reynolds numbers, (850, 1200, 1800, and 2400). The ratios of the maximum velocities in the computational domain during the simulation to the current speeds of the oncoming waves are (from smallest amplitude to largest amplitude) 3.0, 2.9, 3.1, and 2.9. The wave amplitudes (A/A_o) for the simulations are 0.3, 0.45, 0.6, and 0.8, where A_o is the amplitude of a wave that has $\dfrac{\partial \rho_t}{\partial z_T} = 0$ at its steepest point. Other parameters were held fixed in the comparisons. Wave amplitude is an important parameter, influencing both Reynolds number ($Re \sim A$) and Richardson number ($Ri \sim A^{-2}$).

Figure 5 shows that the reflected waves produce much higher velocity currents in the boundary region than occur in the oncoming wave train. The ratio of peak velocities in the boundary region to current speeds in the oncoming waves (U_M/U_w) are similar for different wave amplitudes and Reynolds numbers. These results are similar to results of Ivey and Nokes (1989), who observed maximum velocities of reflected waves of approximately 2 - 3 times the velocities of oncoming waves for a 30^o slope experiment. They determined that the peak velocity in the boundary region, U_M, was a linear function of the oncoming wave amplitude A (Ivey and Nokes, Figure 5b): $U_M = 1.82\omega A + 0.61$. The consistency between

the results of laboratory and numerical experiments, should not be overemphasized, however, in view of differences in the wave amplitudes (Richardson numbers), wave generation mechanisms, and experimental geometries. Nonetheless, it is noteworthy that the maximum velocities occur approximately half a wave period before the peaks in dissipation (*c.f.*, Figure 7).

Figure 6 represents the flow in a different fashion. Here data are presented at a fixed (x_0, y_0) location along the z-direction (ordinate) as a function of time (abscissa) for Case 26. The vertical dimension spans the distance from the bottom boundary to one wavelength (λ_z) away from the wall. The horizontal dimension covers from $t = 30$ to $t = 170$ for a total of 140 time units, equivalent to 7.6 wave periods. The top panel of Figure 6 shows constant contours of the density field; an arbitrary reference value for the constant background density, $\rho_0 = 10$ at $z_T = 0$, has to be added to form the total density field *i.e.*, $\rho_t = \rho_0 + z_T\, \partial\overline{\rho}/\partial z_T + \rho$. In the upper regions of the figure the strongest part of the signal represents the oncoming gravity waves. The variability in the sinusoidal motion here is caused by smaller-scale motions reflected from the turbulent boundary region, which has an approximate thickness of $\lambda_z/3$. In this presentation of the data, the amplitude of the oncoming waves appears quite large; however, this is an artifact of the scale chosen for the horizontal axis. The most significant feature of the flow evident in the top panel of Figure 6 is the periodically strong density gradient near the bottom boundary. This density gradient is the signature of the thermal front, passing through the location of the density probe each wave period. There are seven appearances of the thermal front, corresponding to the seven wave periods during this portion of the experiment. Above the location of the strong gradient are regions of static instability occurring during phases of wave overturning and breakdown.

The bottom panel of Figure 6 shows the corresponding u-component of the velocity field. Solid contours represent upslope flow; the dashed lines represent downslope flow. The strong convergence and divergence associated with the passing of the bore is evident in this figure: the steep density gradient is located where there is a sudden transition from downslope to upslope flow, and hence strong convergence and localized upwelling. After flowing over the

thermal front, the upwelling fluid continues upward and is turned upslope, thereby bringing heavier fluid, located near the boundary, away from the wall into an unstable configuration. Also during the passing of the thermal front, the regions of overturned fluid (located between $0.1\lambda_z < z < 0.3\lambda_z$) experience predominantly upslope flow. The variability in the velocity field indicates the departure of the flow in the boundary region from the regular nature of linear wave dynamics. Farther from the wall the signal of the oncoming waves is present, but significantly smaller than the magnitude of the velocities occurring in the boundary layer.

Figure 7 plots terms of the kinetic (top) and total energy equations (bottom) for the 20^o slope experiment, Case 26, shown in Figures 2-6. The balance, $\overline{B}$, of kinetic energy is very good ($\overline{B}$ and $\overline{W_{KE}}$ are indistinguishable in Figure 7a) and kinetic energy is conserved in the model to a high degree of accuracy. The dominant balance in the kinetic energy equation is between the work input $\overline{W_{KE}}$ and the oscillatory dissipation rate $\overline{\epsilon}$. After approximately $t = 80$, however, the volume integrated buoyancy flux $\overline{B_f}$ becomes large, indicating the strength of the vertical transport occurring both in the boundary layer and in the interior fluid. The period for the buoyancy flux oscillations is 10, or approximately twice per mixing cycle. The buoyancy flux oscillations appear to be more strongly correlated with the wave dynamics than the buoyancy period, which is 2π. While the magnitude of the buoyancy flux seems to suggest a buoyancy driven flow, it is the interaction of the internal wave field with the boundary that creates strong upslope and downslope flows, which in turn makes the dominant contribution to the buoyancy flux. The oscillation in the work input term, $\overline{W_{KE}}$, after $t = 100$ indicates that by this time radiated waves from the turbulent boundary layer have reached upwards into the wave forcing region, which is centered at a height of $z = 2.7\lambda_z$.

The bottom panel of Figure 7 shows the volume integrals of the terms of the total energy equation for Case 26. The total energy equation is the sum of the kinetic and potential energy equations; the buoyancy flux cancels from the sum. The dominant balance in the total energy equation is the nearly steady positive work input balanced by the oscillatory dissipation rate. There is a net gain of energy with time as indicated by the time rate of

change of energy $\overline{E_{TEt}}$ remaining predominantly positive.

The dissipation rates ($\overline{\epsilon} + \overline{\chi}$) are measured separately from the energy removal by the filter, $\overline{F_{KE}}$ and $\overline{F_{TE}}$. The filter accounts for 14% of the kinetic energy dissipation rate and 20% of the total dissipation rate. The quasi-periodic nature of the mixing cycle is evident in the oscillations of the dissipation rate. The first peak in the mixing cycle occurs at $t = 56$ as evident from the maxima in the dissipation rates. Subsequent maxima occur at $t = 80$, 102, 122, 146, and 168, indicating mixing intervals of 24, 22, 20, 24, and 22. These may be compared with the wave period of 18.4.

Case 26, with a bottom slope of 20^o, belongs to the class of flows over shallow slopes, in which the flow has time to restratify and relaminarize between mixing events. Higher frequency flows, such as for a 30^o slope, maintain more uniform levels of total dissipation, as the mixing from one cycle does not decay significantly before the next mixing event begins.

While the flow for Case 26 exhibits characteristics of periodicity, certain aspects also appear to achieve quasi steady state. Figure 8 shows that the volume averages of kinetic, potential, and total energies can either increase steadily or begin to level off after the flow starts up from rest. Two types of situations have been observed in the experiments. In the first, the total energy in the system levels off after a few wave cycles, and the system reaches quasi-equilibrium as the energy oscillates about a mean value (bottom panel); in the second, wave breakdown establishes a mean flow and/or alters the background density profile in the boundary region. The alteration of the background density profile appears in the energy integral as an accumulation of potential energy (even if it is unavailable to do work). An adjustment to the mean flow in the boundary region will appear as an accumulation of kinetic energy. Either of these flow modifications can lead to a steady increase in the total energy in the system.

Figure 8 (top panel) illustrates steady accumulation of total energy in the system. Here, the energy accumulates both as a mean flow and an adjustment to the background density profile (*c.f.*, Figures 18 and 19). Figure 8a (top panel) shows that for the 20^o slope the flow has slightly greater potential energy than kinetic energy during each mixing phase. The

oncoming gravity waves have approximate equipartition of energy (*i.e.,* equal kinetic and potential energies). As kinetic energy is dissipated by turbulence and wall interaction ($\epsilon > \chi$, Figure 7), buoyancy effects transfer excess potential energy to kinetic energy. Also shown in Figure 8 are the time integrated buoyancy fluxes, $\overline{BF} = \int_V \int_0^t Ri\, \rho(w\cos\alpha + u\sin\alpha)\, dt\, dV$; negative values indicate a net transfer of potential to kinetic energy during mixing.

Figure 8 (bottom panel) is for a turbulent critical angle simulation over a 30^o bottom slope (Case 34). In this case, the energy levels in the system achieve quasi-steady values after the startup period ($t > 30$) as the wave train approaches the wall. In this case the energy input from the wave forcing mechanism nearly equals the dissipation of energy when averaged over a wave period. Again the net buoyancy flux is from potential to kinetic energy, but the magnitude of the oscillations between potential and kinetic energy are relatively small.

Figure 9 compares dissipation rates for two critical angle simulations over 9^o and 30^o bottom slopes (Cases 15 and 34). Case 15 was conducted at $Re = 3600$; Case 34 at $Re = 1700$. There is a higher average dissipation rate for Case 15, which is related to the greater energy content of the oncoming waves. Notice the contrast between the cyclical nature of the dissipation rate for the shallow slope case (9.2^o) and the much more constant rate of dissipation for the steep case (30^o). The difference is not attributable to the difference in Reynolds number. Additional simulations conducted over 9^o bottom slopes (*e.g.*, Cases 12-14) at Reynolds numbers between 1200 and 2800 exhibited the same periodic wave breakdown and dissipation (Slinn and Riley 1997a), while less turbulent simulations over the 30^o slope exhibited even more steady dissipation rates. Further details of flow development over a 30^o slope are presented in Slinn and Riley (1997b).

A key distinguishing feature of steep and shallow flows appears to be the ratio of the wave period to the buoyancy period. For ratios greater than about 3:1, the flows are characterized by a thermal front and periodic mixing; for ratios less than 2:1, the thermal front resembles a turbulent bore, which mixes the fluid in a localized region of the boundary layer. Other significant factors, such as wave amplitude and Reynolds number, have lesser influences on the resulting flow distinction.

Figure 10 shows the ratio of the mixing period, T_M, to the wave period, T_w, for critical angle simulations between 3^o and 30^o. Some approximations are involved in estimating the data. For the shallower slopes the results were clearly distinguishable, for example Figure 9 shows three distinct mixing cylces for the 9^o slope. For the 30^o slope Figure 9 shows approximately 15 less-distinct peaks in the dissipation rate between $t = 20$ and 210, for a mixing cycle of 12.6, (which is equal to the wave period). The results at each different bottom slope were averaged over all of the experiments conducted at different Reynolds numbers to arrive at the values plotted in Figure 10. The data show that there are higher ratios of T_M/T_w for smaller slopes. The maximum value observed in the simulations is $T_M/T_w = 1.42$ for the 3.4 degree slope.

The preceding figures have presented results from critical angle simulations representing flows over bottom slopes ranging between 3^o and 30^o. One conclusion from these simulations is that there is a difference between the flow behavior and the nature of the turbulence that develops over shallow versus steep slopes. Previous laboratory studies (Ivey and Nokes, 1989; Taylor, 1993) have focused on internal wave reflection over the steeper slopes, 30^o and 20^o, primarily due to difficulties in designing wave tanks with sufficiently large aspect ratios to examine low frequency waves. An advantage of the numerical approach is that it is possible to perform experiments over the shallow bottom slopes that are more typical of oceanic conditions.

The simulations demonstrate that oncoming waves at the critical frequency break down in a turbulent layer when they reflect from the bottom topography. For the steep slope case (30^o) the flow may be characterized as consisting of a quasi-steady front, which moves upslope at the phase speed of the oncoming wave. The thermal front produces continuous, localized mixing that restratifies behind the front. For the shallower slopes (3^o to 20^o) the flow creates a periodically turbulent layer. In this case, the thermal front appears periodically, especially during phases of initial wave overturning and the onset of breakdown, and reorganizes itself during the phase of relaminarization. For the shallow slopes there is a cycle of strong mixing across the boundary, followed by a period of relaminarization and restratification

of the boundary. The dynamics of the wave breakdown appear to be associated with local upslope/downslope flow induced by the oncoming wave.

3.2 Properties of the Turbulent Layer

3.2.1 Transition

Gaining an increased understanding of transition to turbulence of the oncoming gravity waves has been an aim of the numerical experiments. Table 1 presented flow classifications together with the slopes, frequencies, Reynolds, and Richardson numbers for 34 critical angle experiments. The classification (turbulent, transition, or laminar) was determined primarily by examining the growth of volume averages of components requiring three-dimensionality, such as v^2 and $(\partial w/\partial y)^2$. Simulations with strong positive response during periods of wave breakdown were classified turbulent; weak responses, transitional; and continuous decay of the three-dimensional components, laminar.

Results are presented in Figure 11, which locates flow classification with Reynolds number and slope: seven laminar simulations are plotted with squares, and four transitional simulations are plotted with diamonds. The remaining 23 turbulent simulations are plotted with circles; however, five of the circles are hidden. The trend is for transition and turbulence to begin at lower Reynolds number for increasing slope. For the 3^o and 5^o bottom slopes, transition occurs near $Re = 1800$, whereas for the 30^o bottom slope, transition occurs at approximately $Re = 600$. The intermediate slopes follow this trend, with transition occurring near $Re = 1200$ for the 9.2^o slope. The Richardson numbers for the experiments, are listed in Table 1, and are of similar magnitude for many of the experiments. Thus Richardson number effects are a secondary influence in these experiments in determining the transition point to turbulence.

The influence of higher Richardson number (smaller amplitude waves) is typically to stabilize the flow. For the cases with bottom slope less than 20^o, this generalization holds. For some simulations (7^o, 9^o) the Richardson number varies slightly as a result of lower Reynolds number conditions. (The waves are forced with the same forcing conditions but the more

viscous fluid at lower Reynolds number slightly decreases wave amplitudes as they approach the boundary.) For the cases in which different amplitude waves are generated (3^o, 5^o, 20^o, and 30^o), the results still follow the expected behavior. There are exceptions, however; for example, at 20^o and 30^o some higher Richardson number (more stable) simulations (see Table 1) become turbulent, while other lower Richardson number simulations remain laminar. These exceptions occur, of course, for simulations at higher Reynolds number.

Ivey and Nokes (1989) emphasize another aspect of transition. They suggest that an important parameter to describe transition is the dissipation Reynolds number, $Re_d = \epsilon/\nu N^2$. Results from experiments with a very different mixing mechanism, *i.e.*, grid-generated turbulence (Stillinger *et al.*, 1983; Rohr and Van Atta, 1987; and Itsweire *et al.*, 1986), have suggested a universal transition point for stratified turbulence, *i.e.*, when $Re_d > 10$.

Figure 12 plots gray scale contours of Re_d at two different times for Case 26 with a 20^o bottom slope. Figure 12 shows Re_d in two planes at $t = 75.5$ and 88.9. The top frames are side views (x-z planes) located at $y = 0.5\lambda_z$, and the bottom frames are a top views (x-y planes) located at $z = 0.14\lambda_z$. The darkest contours have values of Re_d exceeding 50, while the lightest regions have contours less than 1. This figure shows that nearly all of the dissipation occurs in the turbulent layer, in both an intermittent and inhomogeneous fashion. The streaks nearest the wall (seen in the top frames of Figure 12) have $Re_d > 700$, while the core of the thermal front has regions with $Re_d \approx 100$. The bottom frames of Figure 12 show the three-dimensional structure of the turbulence. The values of Re_d in this plane range from 0 to 60. While the average values of the dissipation rate are somewhat uniform in the y-direction, the contours of dissipation rate are comprised of strong streaks, indicative of local variability.

The temporal and spatial inhomogeneity of the flow makes it difficult to determine an appropriate average dissipation rate for estimating a total Re_d for the flow. If ϵ is averaged just in the core of the turbulent region at $t = 88.9$, then $Re_d \approx 20$, exceeding the predicted transition value. If, however, ϵ is spatially averaged across the boundary region, to a height of $z = \lambda_z/2$ (including both the viscous sublayer and large regions of low dissipation rate),

then $Re_d \approx 5$. Similar plots from laminar simulations indicate that maximum local values of $10 < Re_d < 20$ are commonly observed in limited regions of the boundary layer for flows that develop and waves that break down in a two-dimensional (*i.e.,* non-turbulent) fashion.

Figure 13 shows horizontally (x-y) averaged value of Re_d as a function of z for Case 26 (top) and Case 34 (bottom) at two different times. These horizontal averages cover both regions of strong dissipation rates (within the thermal front) as well as larger regions of low dissipation rates (in the stratified regions between fronts). Generally the averages suggest values of $Re_d > 10$ for $z < 0.1\lambda_z$ for Case 26, and $Re_d > 10$ for $z < 0.2\lambda_z$ for Case 34 during times of turbulence. These results are in general agreement with the observations of Ivey and Nokes (1989) and others.

Additional figures, not presented here, of potential energy dissipation rates were analyzed. Potential energy dissipation rate contours are very similar in structure to the kinetic energy dissipation rate contours shown, except for the absence of enhanced dissipation rate in the viscous sublayer $z < 0.05\lambda_z$. Shallower slopes increase difficulties in determining appropriate average dissipation rates because of flow intermittencies. Approximately 1/3 of the wave period involves active turbulent mixing. Consequently, the transition rule suggested by Ivey and Nokes (1989), for homogeneous turbulence, must be modified to include temporal and spatial dependencies in order to be extended to the intermittent and spatially inhomogeneous turbulent boundary layers that develop from internal wave reflection. Development of appropriate criteria were considered beyond the scope of this study.

3.2.2 Turbulent layer thickness

Determination of a practical measure for the turbulent layer thickness, δ, is considerably more complicated for the internal wave reflection problem than for simpler types of boundary layer flows. For example, a standard measure of δ for flow over a flat plate is the height to where the boundary layer velocity is $0.99U_\infty$, where U_∞ is the free stream velocity. But the wave driven flows in this study are different, with velocities in the boundary layer typically 2 - 3 times *higher* than the "free stream" velocities (where free stream velocities refer to mean current speeds of the oncoming wave field). In addition, the transition zone (*e.g.,* $\frac{\lambda_z}{3} < z <$

$\frac{2\lambda_z}{3}$) between the boundary layer and the oncoming wave field is temporally and spatially variable. Further complexity is added when radiated gravity waves from the turbulence propagate upwards, passing through and interacting with downward propagating waves. These, and other factors, complicate defining a measure of the turbulent layer depth. One of the advantages in attempting the analysis, however, is that the oncoming waves are two-dimensional (*e.g.*, uniform in the y-direction and containing no v-velocity). Consequently, the variability in the y-direction distinguishes incident waves from responses produced in the boundary layer.

Two different measures of the vertical dependence of the three-dimensionality of the flows are shown in Figure 14. The top frame shows the rms value of the shear rate, $\partial u/\partial y$, for Case 24 over a 20^o slope at four time levels, $t = 48$, 83, 136, and 167. At $t = 48$ the first cycle of wave mixing is just beginning, which gives an indication of the amount of y-variability remaining from the initial background white noise. The vertical axis includes only the bottom vertical wavelength λ_z. For $t > 83$ the flow has experienced a number of stages of the mixing cycle, and the later curves for the shear rate indicate that mixing is strongest in the region $z < 0.3\lambda_z$.

The bottom frame of Figure 14 shows the rms of the v-velocity for Case 34 over a 30^o slope and suggests a more gradual transition between turbulent and wave zones, with a characteristic depth $\delta \approx 0.4\lambda_z$ for the 30^o slope. The strongest generation of v-velocity, associated with turbulence and wave breakdown, is in the region with $z < 0.3\lambda_z$. The v-velocity located above δ is primarily associated with gravity waves radiated from the turbulent region. Thus Figure 14 shows that for both cases three-dimensionality and turbulence occur in the near wall region within a "boundary layer" of approximate thickness $\delta \approx \lambda_z/2$.

Figure 15 suggests still another measure of the boundary layer thickness, and yields δ-values generally in good agreement with the measures already indicated. This method indicates the frequency of static instabilities as a function of distance from the wall. The results are presented for four 30^o slope simulations: Case 28 with $Re = 450$ and $Ri = 490$, Case 30 with $Re = 800$ and $Ri = 625$, Case 31 with $Re = 800$ and $Ri = 156$, and Case

34 with $Re = 1700$ and $Ri = 138$. The results are determined by integrating time series of the density profiles, as shown in Figure 6, at a fixed location. The results indicate that the turbulent layer thickness is approximately $\lambda_z/3$ for the two lower Richardson number cases, and $\lambda_z/6$ for the higher Richardson number case. The lower Richardson number cases used approximately the same wave amplitude, $A \approx A_o/2$, and the difference in Reynolds number was achieved by changing the viscosity of the fluid. The higher Richardson number cases used smaller wave amplitudes, $A \approx A_o/4$ and $A_o/3$, and achieved $Re = 800$ by using a less viscous fluid.

Another set of computational experiments was conducted for the 20^o slope to isolate the effects of adjusting wave amplitude. The wave amplitudes (A/A_o) for these simulations are 0.15, 0.3, 0.45, 0.6, and 0.8, (Cases 18, 21, 23, 24, 27, respectively). Figure 15b (bottom panel) shows that the result of varying the wave amplitude is to change the depth of the turbulent layer. For a regime characterized by higher Richardson numbers, Ivey and Nokes (1989) showed that $\delta \approx 5A$, motivating a similar examination for the present study in which all flow parameters except wave amplitude are held constant. Figure 15b shows the turbulent layer thickness, again measured by the frequency of density inversions by integrating a time series at a fixed location. The approximate depths for the turbulent layers (δ), based upon the heights at which overturned fluid is observed, (from smallest to largest wave) are $0.095\lambda_z$, $0.17\lambda_z$, $0.22\lambda_z$, $0.29\lambda_z$, and $0.36\lambda_z$. (The turbulent layer thickness of the last experiment ($A/A_o = 0.8$) is more approximate than the other values: there is a small region $0.38 < z < 0.42$ that experienced overturning less than 1% of the time, which was considered negligible). The results indicate that as the wave amplitude increases the turbulent layer thickness also increases. The ratios of $\dfrac{A\lambda_z}{A_o\delta}$ for the five cases are 1.58, 1.76, 2.05, 2.0, and 2.2 respectively, so that increases in turbulent layer thickness do not keep pace with increases in wave amplitude.

These results indicate that the turbulent layer thickness is more sensitive to the Richardson number (wave amplitude) than to the Reynolds number for these fairly low Richardson number experiments. Ivey and Nokes (1989) examined a much higher range of Richardson

number (of the order of 10,000 to 100,000) and showed that, in that Richardson number range, the boundary layer thickness is nearly a linear function of the Reynolds number. Numerical simulations of turbulent wave breakdown could not be conducted over a wide enough range of Richardson number to confirm the laboratory result conclusively, but do show general agreement over a limited range. Turbulent layers that develop in the numerical simulations, for large amplitude oncoming gravity waves, have maximum thickness $\delta \approx \lambda_z/2$. This may provide an upper bound for the depth of the turbulent layer in oceanic flows generated by wave reflection, given the large amplitude of the waves and the insensitivity of the result to Reynolds number.

3.2.3 Particle Diffusion

Lagrangian particles were followed in the flow to examine fluid exchange between the boundary region and the interior stratified fluid. Depending on the phase of the wave and turbulence in the boundary layer at the location of each particle, the particles initially move either upward or downward. If the particles are released in a region of linear wave dynamics then, after one wave period, each would return approximately to its initial locations. This behavior is approximated for particles started at $z > 2\lambda_z$. Particles initially released in a region of turbulence do not return to their initial location after a wave period. After each additional wave period the particle dispersion increases and appears to be more random. At intermediate heights ($0.7\lambda_z < z < 1.5\lambda_z$) the motion is a combination of wave motion and mean current drift. While the particles fail to return to their initial locations, neither do they follow the complicated three-dimensional trajectories seen in the turbulent layer. Results indicate that the average vertical distance traveled by a fluid particle over one-half wave cycle is approximately $0.2\lambda_z$, *i.e.*, a particle moves upwards $0.2\lambda_z$ during the upward phase of wave motion and returns $0.2\lambda_z$ downwards during the downward phase, in agreement with linear theory.

The net effects of particle dispersion are quantified in Figure 16. The calculations were carried out for approximately 3 wave periods for Case 24 (from $t = 74$ to $t = 134$). Each data point represents the average of a set of 200 particles released uniformly across a plane

parallel to the wall at the specified heights $z = z_0$. The net effects of the phases of the wave that are first encountered by the particles (upward or downward motion) are eliminated from the average by distributing sufficient numbers of particles spatially so that all of the wave phases are included. No attempt was made here to distinguish upward from downward displacements. The largest total displacements occur for particles released at middepth in the turbulent layer, with average vertical displacements of approximately $0.32\lambda_z$ after about 3 wave periods. Smaller average displacements occur for particles closer to the wall than approximately $0.17\lambda_z$, and for those initially farthest from the wall.

Figure 16 translates the mean particle motion into a depth dependent diffusion coefficient defined by $D(z_o) = \frac{1}{2}\frac{\partial\overline{(z-z_o)^2}}{\partial t}$, (Tennekes and Lumley, 1972; Fuchs, 1964) where $\overline{(z-z_o)^2}$ is the mean square vertical particle displacement averaged over a set of particles released from an initial height z_o. The time derivatives are estimated using linear regression analysis over three wave periods of particle displacements. The results for $D(z_o)$ are plotted at ten vertical locations between $0 < z < 0.7\lambda_z$. The strongest diffusion occurs for particles initially released between $0.1\lambda_z < z < 0.2\lambda_z$. Above the turbulent boundary layer at heights $0.4\lambda_z < z < 0.7\lambda_z$ the rate of turbulent diffusion is approximately constant and about one-third the value in the regions of strongest turbulence. At still greater heights, $z > 1.5\lambda_z$ (not pictured), the diffusion coefficients decrease to less than half the value at $z = 0.7\lambda_z$. Generally, the results from the particle experiments support the view that there is significant net vertical transport of fluid in the simulations.

3.2.4 Wall Shear Rates

Interest in wall shear stresses caused by internal wave reflection is motivated by two important oceanic considerations. The first is the effect on the sea-bed itself, and especially on the relationship to sediment transport. Depending on the type of sediment on the boundary, currents generated by internal wave breakdown may be sufficiently strong to suspend and/or move sediment from one location to another. Cacchione and Drake (1990) and Southard and Cacchione (1972) have examined in the laboratory and in the field (Cacchione *et al.*, 1988) the movement of sediment caused by shoaling internal waves. A second issue related

to strong wall shear is the effect of suspended particles on the water. Two potentially important effects of particle suspension are changes to the optical properties of the water column (Cacchione and Drake, 1986) and modifications to the turbulence (because the concentration of sediment in the water changes the effective density stratification).

Figure 17 show contours of wall shear component $\partial u/\partial z|_w = \tau_{xz}/\mu$ for Case 26 (20^o slope) at $t = 77.1$ and 172. Also shown for comparison is the shear in an x-y plane parallel to the boundary at a height $z = 1.4\lambda_z$; this indicates the relative magnitude of the shear contained in the oncoming internal wave. The component of the wall shear in the y-direction, $\partial v/\partial z|_w$, (not pictured) is typically one-half the magnitude of the wall shear in the x-direction.

Predominantly, downslope flow is indicated by the negative (dashed) contours and upslope flow by positive (solid) contours. At $t = 77.1$ the spatial variation is primarily two-dimensional. Positive contours in the top panel occur at the locations of the two thermal fronts. At $t = 172$ the flow is in a period of mixing, and the turbulence in the fluid has caused the wall shear to become more three-dimensional. Contour levels of the wall shears range from -30 to 30.

These values may be compared with the shear in the oncoming wave as it approaches the boundary layer, having values ranging from approximately -0.3 to 0.3. That is, the shear at the wall is approximately 100 times higher than the shear in the oncoming wave. This strong amplification of wave shear is caused by amplification of wave currents in the vicinity of the boundary, compression of the vertical length scale of the reflected wave, and the presence of the viscous layer associated with the no-slip boundary condition.

Results from several different experiments show that wall shears caused by critical internal wave reflection are from one to two orders of magnitude higher than the shear of the oncoming wave. Strong shears, coupled with strong local upwelling features of near boundary fluid (such as flow over the thermal front), can cause resuspension of bottom sediment. While the strongest shear rates are localized, they pass across the boundary each wave period. The simulations support conclusions of other researchers that internal wave reflection may make significant contributions to fluid-sediment boundary interactions.

3.2.5 Changes to Background Field

In the model problem and its oceanic counterpart, an issue of considerable interest is the long term response of the background when modified by wave breakdown and mixing in the turbulent layer. Two significant results that may appear are changes to the background density profiles and creation of mean currents. Each of these flow adjustments are indicators that net mixing effects are communicated to the interior stratified fluid.

Profiles of the horizontally (perpendicular to gravity) averaged density for Case 26 (20^o slope) are shown in Figure 18 at $t = 5.9$, 84.8, and 172 as a function of z_T (parallel to gravity). An arbitrary reference value for the constant background density, $\rho_0 = 10$ at $z_T = 0$, is added in Figure 18 to form the total density field before averaging the values, *i.e.*, $\rho_t = \rho_0 + z_T\, \partial\overline{\rho}/\partial z_T + \rho$. The (x, y, z) and (x_T, y, z_T) coordinate systems intersect at the origin $(0, 0, 0)$. The horizontal averaging process nearly eliminates the density structure of the oncoming waves, which are periodic in x but only approximately periodic in x_T. Horizontal averaging is done on the intervals $0 \le y \le \lambda_z$ and $0 \le x_T \le 2\lambda_x$ for $z_T > 2\lambda_x \sin\alpha$, and for $0 \le x_T \le x_W$ for $z_T < 2\lambda_x \sin\alpha$ where $x_W = z_T/\tan\alpha$ is the location of the sloping boundary.

The initial density profiles ($t < 30$) are approximately linear when only oncoming waves are present. After three to four mixing cycles, adjustments to the initial profile have reached a height of at least $z_T = \lambda_z$. By $t = 85$ layering of the mean density profile is evident. At $t = 85$ for $0.2\lambda_z < z_T < 0.4\lambda_z$ and $0.6\lambda_z < z_T < 0.8\lambda_z$, the density gradient is weaker than the original linear profile. Associated with these layers are intrusions of mixed fluid that propagate into the interior stratified region from the boundary layer. Between the more homogeneous layers, at $0.4\lambda_z < z_T < 0.6\lambda_z$, is a layer of increased density gradient. For $t = 172$ the most homogeneous mixed layers are observed at $0.3\lambda_z < z_T < 0.6\lambda_z$ and $0.8\lambda_z < z_T < 1.1\lambda_z$, and the density structure exhibits layering to heights approaching $z_T = 1.5\lambda_z$. This type of layering of the density profile was observed for most turbulent simulations with $\alpha < 20^o$.

At the times shown in these figures the density gradients may vary locally by approxi-

mately $\pm 50\%$ from the initial profile. As the profiles change, the local buoyancy frequency, N, will also change, possibly resulting in a progressive mismatch between the angle of propagation of the oncoming waves $\theta(\omega, N)$ and the bottom slope. Oceanic conditions imply that a vast reservoir of stratified fluid exists in proximity to the sloping boundaries, providing a sufficient source to restratify the boundary region between mixing events for extended periods of time, as long as horizontal mixing is effective.

Additional evidence of the layering of the fluid is revealed in Figure 19. Here, a passive "dye" has been released in the near wall region at $t = 0$, and is followed through approximately eight mixing cycles for Case 26. The initial concentration, C, of the dye near the boundary is $C = 1.0$ for $z < 0.15\lambda_z$, falling off between $0.15\lambda_z < z < 0.25\lambda_z$, and $C = 0$ for $z \geq 0.25$. As mixing occurs in the turbulent layer the concentration of dye near the wall decreases. Concentration levels of $0 < C < 0.5$ are plotted in Figure 19 at $t = 0.6$, 88.9, and 172. Horizontal intrusions of dye are observed to steadily work their way into the interior domain, approximately following surfaces of constant density. At $t = 172$ two distinct horizontal dye layers are evident, located at $z_T \approx 0.7\lambda_z$ and $z_T \approx 1.1\lambda_z$. Each of these layers extends from a different horizontal wavelength of the oncoming waves. By $t = 172$, approximately eight wave periods after mixing in the boundary layer begins, the dye has extended approximately two horizontal wavelengths into the interior flow from the turbulent boundary layer.

Using video we have found that the location of the dye layer oscillates in its vertical position as the oncoming waves pass through it. The motion occurs in a reversible fashion, lifting and falling through different phases of the oncoming wave. The dye propagates into the interior through mean currents induced by the breaking waves. A steady circulation driven by buoyancy forces is created as a net result of the boundary mixing. We conclude that the net effects of boundary mixing are not confined to the boundary layer region but are communicated horizontally to the interior stratified fluid.

Interestingly, the 30^o slope does not show the same degree of adjustment to the interior density stratification as do the shallower slopes (Slinn and Riley, 1997b). In this case, instead

of well defined intrusions of intermediate density fluid at specific depths, what appears is a uniform thickening of the dye layer along the slope. The reasons for the difference are not readily apparent but may be attributed to more localized mixing occurring at all depths as the turbulent bore passes upslope.

A significant feature of the boundary mixing process is that the internal wave field outside the turbulent region plays a very active role. It serves to continuously pump fresh stratified fluid into the mixed layer, while simultaneously extracting the mixed fluid. This process is suggested by the strong internal wave shear seen in the velocity fields in Figure 3. This exchange of boundary mixed and stratified fluid is referred to as internal wave pumping. These results suggest that the wave field is important in first communicating the boundary mixed fluid into the interior stratified regions, and that the mixed fluid is further transported into the interior along constant density surfaces due to hydrostatic imbalance. Internal wave pumping of fresh fluid into the boundary layer and the simultaneous extraction of mixed fluid is an important immediate link between the two regions.

3.3 Mixing Efficiencies

In this section's analysis of the simulations, emphasis is placed on energetics of the flows. A quantity of particular interest is the mixing efficiency, which in general is related to the portion of wave energy that goes to irreversible mixing of the density field. In this section, first, the numerical simulations are analyzed, and second, some new, exact solutions to the Navier-Stokes equations are presented that give insight into mixing.

In the present numerical experiments, the mixing efficiency is represented as the ratio of the potential energy dissipated to the work input to generate the oncoming waves,

$$\eta = \frac{-\int_{t_i}^{t_f} \left[\overline{\chi} + \overline{F_{PE}}\right]\, dt}{\int_{t_i}^{t_f} \overline{W_{TE}}\, dt} \,. \tag{3.1}$$

The values of $\overline{\chi}$, $\overline{F_{PE}}$, and $\overline{W_{TE}}$ are volume integrated over the full domain from the time when the oncoming wave train has reached the boundary, t_i, until the end of the simulation, t_f.

Because $\overline{\chi}$ oscillates throughout the mixing cycle, while the work input remains almost constant, the resulting value of η oscillates about a mean value over each mixing cycle, but the oscillations dampen in time as the respective integrals become larger. For most experiments the ratio of the integrals of $-\left[\overline{\chi} + \overline{F_{PE}}\right]$ and $\overline{W_{TE}}$ quickly achieve stable values after the wave train reaches the boundary. For each of the simulations, the best approximation for t_i was chosen based upon energetics and flow visualizations, and the sensitivity of the result on η was examined to arrive at a best estimate for the mixing efficiency. This method of determining the rate that available potential energy is irreversibly converted to background potential energy is only approximate (Winters *et al.*, 1995) but is sufficient for the purposes of this investigation. Alternatively, the mixing efficiency in oceanic field observations is usually defined as $\eta_2 = \int_t \overline{\chi}\, dt \,/\, \int_t (\overline{\chi} + \overline{\epsilon})\, dt$ in accord with laboratory-based measurement. These two definitions for η are closely related for flows which dissipate nearly all of there initial energy (or for flows in steady state), so that $\overline{\chi} + \overline{\epsilon}$ is approximately equal to the total energy (or energy flux) in the flow. In the simulations the values of η_2 are typically 10% larger than the values of η and show the same trends.

Table 2 presents the mixing efficiencies, heat gain coefficients, and radiation coefficients for Cases 1 - 34. The heat gain coefficient is defined, similar to the mixing efficiency, as the ratio of the integrals of the kinetic energy dissipation rate to the work input,

$$H = \frac{-\int_{t_i}^{t_f} \left[\overline{\epsilon} + \overline{F_{KE}}\right]\, dt}{\int_{t_i}^{t_f} \overline{W_{TE}}\, dt}\,. \tag{3.2}$$

The radiation coefficient, R, is inferred from the remainder of energy not dissipated as either heat or mixing, *i.e.*, $R = 1 - \eta - H$. For these critical angle simulations, carried out over a range of Reynolds numbers, the mixing efficiencies are near 0.35. Thus, a typical energy budget for the oncoming waves is that approximately 35% of the oncoming wave energy goes into mixing the stratified fluid, approximately 55% is dissipated as heat, and (thus it may be inferred that) approximately 10% of the incident energy is reradiated away from the turbulent boundary layer by smaller scale gravity waves or induced mean currents.

The error bars on the results are approximately ± 0.02 based upon the subjectivity introduced by choosing t_i and t_f for the integrations of $\overline{\chi}$, $\overline{\epsilon}$, and $\overline{W_{TE}}$. There is no obvious

dependency of the mixing efficiency on either Reynolds number or bottom slope, but for a given bottom slope, the lower Reynolds number simulations appear to radiate less energy away from the boundary layer. While one might assume that higher Reynolds number flows should generally be more efficient at mixing, the analysis in the next section suggests that low Reynolds number internal waves have mixing efficiencies of 0.5 (for a Prandtl number of 1.). Thus, the separation of laminar from turbulent dissipation rates may be ineffective in the simulations. Mixing efficiencies for off-critical frequency waves will be described in the following section.

Figure 20 plots the values of mixing efficiency (circles), heat gain coefficient (diamonds), and radiated energy for the simulations listed in Table 2. There appear to be weak general trends, indicating lower "average" mixing efficiencies, somewhat higher heat gains, and less radiation of energy for the steeper slope simulations. The trends should not be overemphasized, however, as the "averaging" may be inappropriate for the wide range of Reynolds numbers and different types of flow development that occur (*e.g.*, laminar, turbulent, steady, intermittent). The spread in the data is considerably larger than the variation in the overall trends and should therefore be considered inconclusive.

3.3.1 Prandtl Number Dependence

To further understanding of mixing efficiencies in these numerical simulations it is important to learn as much as possible from any exact solutions for an internal gravity wave propagating in a viscous fluid. While the following derivations appear to be straightforward, they do not appear to have been published previously.

Beginning with the three-dimensional Navier Stokes equations within the Boussinesq approximation, as given in Equations (2.1) - (2.5) with $\alpha = 0$, we seek a plane-wave solution with $v = 0$, allowing the problem to be examined in two dimensions. The nonlinear terms are all identically zero for plane waves, and the dispersion relation becomes

$$\omega = i\omega_I + \omega_R \,, \tag{3.3}$$

where

$$\omega_I = \frac{-1}{2}\left[\frac{k^2+m^2}{Re\,Pr} + \frac{k^2+m^2}{Re}\right] , \tag{3.4}$$

and

$$\omega_R = \left[\frac{Ri\,k^2}{k^2+m^2} - \frac{1}{4}\left(\frac{k^2+m^2}{Re\,Pr} - \frac{k^2+m^2}{Re}\right)^2\right]^{1/2} , \tag{3.5}$$

which has the limit for $Pr = 1$,

$$\omega = -i\,\frac{k^2+m^2}{Re} + \frac{\sqrt{Ri}\,k}{(k^2+m^2)^2} , \tag{3.6}$$

and for $Pr \to \infty$,

$$\omega = \frac{-i}{2}\frac{k^2+m^2}{Re} + \left[\frac{Ri\,k^2}{k^2+m^2} - \frac{1}{4}\left(\frac{k^2+m^2}{Re}\right)^2\right]^{1/2} . \tag{3.7}$$

Consequently, the time-dependent flow field for a viscously-decaying, nonlinear internal gravity wave is described by

$$w(x,z,t) = Ae^{\omega_I\,t}\,\cos\phi\,, \tag{3.8}$$

$$u(x,z,t) = \frac{-Am}{k}\,e^{\omega_I\,t}\,\cos\phi\,, \tag{3.9}$$

$$\rho(x,z,t) = \frac{A}{2}\left(\frac{k^2+m^2}{Re\,Pr} - \frac{k^2+m^2}{Re}\right)\frac{k^2+m^2}{Ri\,k^2}\,e^{\omega_I t}\cos\phi$$

$$-A\left(\frac{k^2+m^2}{Ri\,k^2}\right)\left[\frac{Ri\,k^2}{k^2+m^2} - \frac{1}{4}\left(\frac{k^2+m^2}{Re\,Pr} - \frac{k^2+m^2}{Re}\right)^2\right]^{1/2} e^{\omega_I t}\sin\phi\,, \tag{3.10}$$

where $\phi = (kx + mz - \omega_R\,t)$. The results are valid for any wave amplitude, A, as no assumptions were made in the derivation restricting the result to linear or small amplitude waves.

These results are used to investigate the energetics of a decaying wave. The kinetic energy, $KE = (u^2+w^2)/2$, potential energy, $PE = Ri\,\rho^2/2$, and the buoyancy flux, $B_f = Ri\,\rho\,w$, averaged over a wave period are,

$$\overline{KE}(t) = \frac{A^2\pi}{2}\,e^{2\omega_I t}\left(\frac{k^2+m^2}{k^2}\right) , \tag{3.11}$$

$$\overline{PE}(t) = \frac{A^2\pi}{2}\,e^{2\omega_I t}\left(\frac{k^2+m^2}{k^2}\right) , \tag{3.12}$$

$$\overline{B_f}(t) = \frac{A^2\pi}{2}\, e^{2\omega_I t} \left(\frac{k^2+m^2}{k^2}\right) \left(\frac{k^2+m^2}{Re\, Pr} - \frac{k^2+m^2}{Re}\right) \ , \tag{3.13}$$

where $\overline{(\ )}$ denotes a spatially integrated value.

The most significant use of these solutions for the current purposes is to examine χ and ϵ and their ratio. Spatially integrating over wavelengths gives

$$\overline{\epsilon}(t) = \frac{A^2\pi}{Re}\, e^{2\omega_I t} \left(\frac{k^2+m^2}{k}\right)^2 \ , \text{ and} \tag{3.14}$$

$$\overline{\chi}(t) = \frac{A^2\pi}{Re\, Pr}\, e^{2\omega_I t} \left(\frac{k^2+m^2}{k}\right)^2 \ . \tag{3.15}$$

The result shows that the ratio $\overline{\epsilon}/\overline{\chi} = Pr$ is proportional to the Prandtl number. Note, in particular, that for comparison with the numerical simulations conducted in this study, for $Pr = 1$, then $\overline{\chi} = \overline{\epsilon}$ for the internal wave. These exact results can be translated into a mixing efficiency, here using $\eta_2 = \overline{\chi}/\left(\overline{\chi} + \overline{\epsilon}\right) = 1/\left(1 + Pr\right)$, which is graphed in Figure 21. Thus for $Pr = 1$, the mixing efficiency is 0.5. This is the primary result of this section. Physically the result means that a viscously decaying internal gravity wave with $Pr = 1$ dissipates kinetic and potential energy at the same rate.

Our exact solution is valid for plane waves at all Reynolds numbers. The rate of viscous decay of energy in a plane gravity wave decreases rapidly with increasing Reynolds number [see Equations (3.4) and (3.11)], while the same quantity in a turbulent flow is approximately independent of Reynolds number. It is therefore desired to compare the dissipation rates caused by viscous decay of internal waves in the simulations to dissipation rates caused by turbulence. At high Reynolds number, the dissipation due to turbulence may be much larger than viscous dissipation for internal waves; but for low and moderate Reynolds number flows, such as those conducted in the simulations, the viscous (laminar) dissipation of energy of the internal waves may be comparable to dissipation caused by turbulence. To preserve adequate numerical resolution of the small density structures that develop, Prandtl numbers of $O(1)$ are used in the simulations. A complication that arises from this constraint is that the dissipation rates of kinetic and potential energy are approximately equal for the internal wave, and influence the resulting determination of η by driving it towards 0.5.

Rehmann and Koseff (1994) have described Prandtl number dependence on mixing efficiency for decaying grid-generated turbulence. For the Reynolds numbers in their laboratory experiments they find that Prandtl number effects are small, but their analysis shows that, for higher Richardson numbers, Prandtl number effects may become important for smaller Reynolds numbers.

Turbulent dissipation rates of both kinetic and potential energy are expected to be higher than laminar values. In the numerical simulations, we observe values near 0.35 instead of 0.5. The reason is partially related to the influence of the no-slip boundary condition at the wall. In the viscous sublayer, strong dissipation of kinetic energy occurs; this has no counterpart in dissipation of potential energy because of the no-flux boundary condition on the density field. In these simulations, additional analysis (not presented) focusing only on the turbulent layer ($0.1\lambda_z < z < 0.4\lambda_z$) indicates that dissipation rates of χ and ϵ are approximately equal. Thus, it might be expected that low Reynolds number simulations conducted for a free-shear flow, remote from the presence of a boundary, would have mixing efficiencies near 0.5 (for $Pr = 1$).

When $Pr > 1$, the internal wave loses more kinetic than potential energy. For the wave to retain its wave structure (including equipartition of energy), there is a compensating buoyancy flux from potential to kinetic energy. Figure 22 compares results for $\overline{\chi}$, $\overline{\epsilon}$, and $\overline{B}_f$ as a function of Prandtl number. Parameters for this plot are: $k = 2\pi/1.5$, $m = 2\pi/0.7$, $A = 0.1$, and $Re = 1000$. For Prandtl numbers below one, $\overline{\chi}$ is greater than $\overline{\epsilon}$, so that the wave loses more potential than kinetic energy. In this range, therefore, the buoyancy flux is positive, transferring excess kinetic to potential energy. For $Pr > 1$, the opposite is true: as more kinetic energy is dissipated, the deficit is resupplied by a negative buoyancy flux, transferring potential to kinetic energy. Note that the magnitude of the buoyancy flux is exactly $(\overline{\chi} - \overline{\epsilon})/2$.

This section on mixing efficiencies is concluded by comparing the theoretical results with numerical results obtained for turbulent internal wave reflection experiments for Prandtl numbers between 0.6 and 2. These numerical results support the suggested trends of the

importance of Prandtl number effects on turbulent mixing dynamics. It should be noted, however, that for turbulent dynamics at high Reynolds number, ϵ and χ are thought to be controlled by the rate of transfer of energy to small scales. A linear theory would not predict this dependency and may only be useful at lower Reynolds numbers.

The results of three numerical experiments, Cases 15-17, of critical angle reflection for $\alpha = 9.2^o$, $Re = 3600$, $Ri = 46$ are presented in Figure 23. The mixing efficiencies fall into a relatively narrow range, with values of $\eta = 0.38$, 0.32, and 0.27 for Prandtl numbers of 0.6, 1.0 and 2.0 respectively. The heat gain coefficients are 0.50, 0.56 and 0.62, so that radiation from the boundaries are essentially equal for all three turbulent wave breakdown experiments: 0.12, 0.12, and 0.11. Using the second definition for the mixing efficiency, $\eta_2 = \int_t \overline{\chi}\, dt / \int_t (\overline{\chi} + \overline{\epsilon})\, dt$, the experiments have values of $\eta_2 = 0.43$, 0.36, and 0.30, which may be compared with results for the viscously decaying internal wave: the predicted mixing efficiencies for these Prandtl numbers are $\eta_2 = 0.62$, 0.5, and 0.33. Consequently, it appears that turbulent dynamics are a significant factor in lowering the mixing efficiencies in the internal wave reflection experiments, but it is difficult to determine their overall influence from Reynolds and Prandtl number effects.

The conclusion is that the Prandtl and Reynolds numbers are significant in determining mixing efficiencies in low to moderate Reynolds number simulations. Numerical simulations are useful for understanding key physical processes in fluid flows, and for determining qualitative and semi-quantitative estimates of flow behavior as well as trends for different parameter values. They will not, however, produce the same values for mixing efficiencies as measured in related laboratory and field experiments until appropriate Prandtl and Reynolds numbers can be used in the numerical simulations, *i.e.*, until more computational speed and memory become available.

3.4 Off-Critical Angle Results

A series of simulations was conducted to examine flow behavior for oncoming waves with angles of propagation away from the critical angle. In this set of experiments the frequency

of all oncoming waves is $\omega = 0.16$, so that the angle of wave propagation with respect to the horizontal is 9.2^o. The bottom slope was varied in the simulations between 0^o and 13.5^o. For the simulations conducted with bottom slopes between 0^o and 9.2^o the waves reflect upslope. This is called supercritical reflection, because the wave frequency is higher than the frequency of a wave propagating at the critical angle associated with the bottom slope. For simulations conducted with bottom slopes of 9.2^o and above, the waves reflect downslope (subcritical). The series of off-critical angle simulations are listed in Table 3, which identifies the case number, bottom slope, Reynolds and Richardson numbers, amplification factor (from linear theory), the ratio of the maximum observed velocity in the boundary region to the oncoming wave current speed, U/U_M, and the classification of each simulation (*e.g.*, laminar or turbulent).

Simulations conducted over a flat bottom ($\alpha = 0^o$) were used primarily for reference to other simulations. An additional complication was introduced into the two flat-bottom simulations by using two different types of boundary conditions for density. The first one (Case 35) used a no-flux (adiabatic) boundary condition (as did all of the simulations over sloping boundaries). For a sloping boundary the no-flux condition produces a steady secondary flow (Phillips, 1970), maintained by a balance of advection and diffusion, by establishing buoyancy-induced boundary currents. For a flat bottom, however, the no-flux boundary condition does not result in the establishment of boundary currents, and the depth of the boundary region influenced by diffusion grows steadily, weakening the stratification near the boundary. This effect was somewhat removed from the simulation in Case 30 by using a constant density (isothermal) boundary condition. While this condition also influences the flow near the boundary, the effect appears smaller than from the no-flux condition, facilitating comparison with the sloping boundary simulations.

The simulations with 5^o and 13.5^o bottom slopes were chosen to complement one another, because one is approximately 4.2^o above and the other 4.2^o below the critical angle (9.2^o). Similarly, the simulations at 8^o and 10.5^o are approximately 1.25^o on either side of critical.

In certain respects, the off-critical angle simulations contain more complexity than the

critical angle simulations. The main difference is that the energy of the oncoming wave is not confined, upon reflection, to the boundary region but reflects away from the slope. The process is illustrated, using linear ray theory, in Figure 1. The reflected wave passes through the oncoming wave, allowing the possibility of wave-wave interactions to occur remote from the boundary. Thorpe (1989) and Thorpe and Haines (1987) have used weakly nonlinear resonance theory to examine interactions between oncoming and reflected wave trains. The present numerical simulations have showed evidence of the formation of a third wave, caused by near-resonance interactions between oncoming and outgoing waves, for reflection from a 5^o bottom slope for a small amplitude simulation (Slinn, 1995).

Table 3 lists values of the ratio of the maximum velocity observed during the simulation in the boundary region to the maximum current speed in the oncoming wave train. These ratios were observed between approximately 1.5 and 2.6. For each different bottom slope, higher ratios generally occur for higher Reynolds number simulations, with exceptions over the 5^o and 10.5^o slopes which have the highest ratios at intermediate Reynolds number.

An issue examined with the present set of simulations is how close to the critical angle an oncoming wave must be to cause similar mixing. Table 4 presents results for the energy budgets of the off-critical simulations. This table lists approximate mixing efficiencies, heat gain coefficients, and radiation coefficients (representing wave energy that radiates away from the boundary or causes changes to the background flow). As described in Section 3.3, the energy values are determined after the oncoming waves have reached the bottom boundary and a quasi-steady process has commenced.

The results from Table 4 are plotted in Figure 24, which locates the values of the mixing efficiency, heat gain, and radiation coefficient as a function of slope. The trend is towards smaller radiation for larger slopes. It is likely that the experiments close to critical angle were not conducted for long enough duration for a quasi-steady state to be achieved. Typically these experiments were only conducted for between 5 and 8 wave periods. At larger slopes (*i.e.*, 20^o - 40^o) reflection would be expected to be similar to the limit that exists for a flat-bottom (*e.g.*, reflection from a vertical boundary is the same as from a horizontal boundary).

The result is that the average values for the reflection coefficient should rise for steeper slopes.

These off-critical angle simulations reveal a range of radiation of energy of more than a factor of 3 between the highest and lowest values, depending largely upon the Reynolds number. If additional simulations were conducted at other Reynolds numbers for the 13.5^o slope, it would not be surprising to find a broader distribution for the radiation coefficient.

As seen in Figure 24, the radiation coefficient for the flat bottom case is approximately 0.3. For inviscid (linear) waves this value would be approximately 1.0. This difference illustrates the significant viscous losses of energy experienced by waves for the moderately low Reynolds number conditions of these cases (Re = 620, 1250). To examine different regions of wave-energy loss, consider the following three-stages of wave reflection: approach toward the boundary (within a height of approximately $2\lambda_z$), reflection and interaction with the viscous sublayer (thickness of approximately $0.1\lambda_z$), and propagation away from the boundary (to a height of approximately $3.5\lambda_z$). Proportions of wave energy lost in each stage for these Reynolds numbers can be approximated by examining the energetics at different stages of the transient flow development. The results are that approximately 20% of the wave energy is lost while approaching the boundary, 25% is lost near the boundary, and an additional 25% (for a total of 70% dissipated and the remaining 30% passing out of the top of the domain through the upper open boundary) is lost after reflecting from the boundary. For the higher Reynolds number experiments ($\sim$ 3600), the viscous losses may account for approximately 30% of the total wave energy. The results also depend somewhat on the angle of wave propagation, θ, or, in the model, more precisely, $\theta + \alpha$. For larger values of $\theta + \alpha$ the waves approach the boundary more rapidly and less energy is lost to viscous dissipation. Note also that the waves propagate at a shallow (9.2^o) angle to the horizontal, so that they travel approximately six times farther in the horizontal than in the vertical direction.

From Table 4, Figure 24 also locates values of mixing efficiency and heat gain coefficients as a function of the slope. Figure 24 implies that waves reflected from steeper slopes have lower radiation coefficients because of higher losses to heat rather than higher mixing efficiencies. The mixing efficiencies are generally highest close to the critical angle, but, as seen

by the spread in the data at the critical angle, the mixing efficiencies depend on Reynolds number as strongly as they depend on slope. The simulations indicate that the integrated energetics for the 8^o and 10.5^o slopes are essentially the same as the energetics at the critical angle. The simulations at 5^o and 13.5^o are dissimilar from one another and from the critical angle results.

The off-critical experiments indicate that the duration of the mixing cycles varies with the bottom slope. All the simulations used waves with the same frequency and wave period ($T_w = 39.1$). As noted before, critical angle simulations typically have a mixing cycle approximately 10 - 40% longer than the wave period. Observations of off-critical angle simulations show that the mixing cycle is shortened for slopes above and lengthened for slopes below critical.

Table 5 shows the duration of the mixing periods as a function of slope. The values are averages from a number of simulations at each slope. Because reflection from a flat bottom is observed to become steady and no mixing cycle is observed (except if reflected waves interact nonlinearly with oncoming waves), the mixing period, T_M, for the flat bottom case is listed as infinite. Also included for comparison in Table 5 are the wave period for a critical frequency wave, T_{W_c}, for each bottom slope, and the ratios of the mixing periods for the off-critical waves to the wave periods of the critical frequency waves, T_M/T_{W_c}. Note that the mixing cycles for the off-critical waves (all with wave periods of 39.2) follow a similar trend to the wave periods for critical frequency waves for the other slopes. These results show that supercritical reflection has significantly longer mixing cycles than subcritical reflection.

The flow fields for the 8^o and 10.5^o slopes are essentially the same as the flow fields that develop for critical angle simulations of similar Reynolds number. Flow fields farther from the critical angle, however, develop in different manners. Figure 25 presents isopycnals of the flow for Case 39 ($Re = 2300$, $\alpha = 5^o$) at $t = 130$, 184, 249, and 270; and Case 50 ($Re = 2120$, $\alpha = 13.5^o$) at $t = 92$, 111, 119, and 140. The initial flow development for each experiment shows that a thermal front develops in the boundary layer, similar to the critical angle simulations. The density fields that develop during the mixing cycle, however, are somewhat different from those that develop for critical angle reflection. Also, while both the

simulations at 5^o and at 13.5^o are $\pm 4.2^o$ from the critical angle, the flows that develop (for similar Reynolds and Richardson numbers) are qualitatively different from one another. For the steeper slope, the region of wave overturning and breakdown occurs above and behind the thermal front in a comparatively broad region. For the shallower slope less frequent wave overturning occurs for similar amplitude oncoming waves, and the region of strongest wave-wave interaction is predominantly above and ahead of the thermal front. The localized regions of wave overturning are consistent with the respective directions (upslope/downslope) of wave reflection.

Eriksen (1985) theorizes that a difference in character for subcritical and supercritical reflection should exist, suggesting that reflected waves interact with the oncoming waves in different manners, leading to different mixing characteristics. He calls supercritical reflection (*e.g.*, our 5^o case) transmissive and subcritical reflection (*e.g.*, 13.5^o) reflective. A difference is observed in the numerical simulations and indicates that, in the supercritical case, the reflected waves pass through the oncoming waves in a constructive fashion. In the subcritical case, the reflected waves interfere with the oncoming waves in a more destructive fashion (leading to turbulent mixing). The essential difference is that the oncoming and reflected waves are out of phase with one another, causing wave breakdown to be facilitated.

In summary, it was found that off-critical angle reflection is a complicated process and that this angle is an additional parameter that governs flow development. The angle of the bottom slope influences wave reflection by lengthening the mixing cycle for cases with shallower slopes and shortening the mixing cycle for those with steeper slopes. Wave reflection and breakdown develop in a very similar manner to the critical-angle situation for both subcritical and supercritical waves close to the critical angle. For cases farther from the critical angle, there is an asymmetry to the flow development: subcritical reflection experiences increased dissipation rates to heat and mixing, while supercritical reflection has a higher component of radiation of energy away from the boundary.

4 Summary

Several aspects of the internal wave reflection problem have been addressed. Transition to turbulence has been determined to be a function of bottom slope, Reynolds number, and Richardson number. An average value for the Reynolds number at transition, from the mid range of values of bottom slope and Richardson numbers in these experiments, is approximately $Re = 1000$ based upon the wavelength and maximum wave current speed. The resulting turbulence has also been examined, especially in terms of its mixing efficiency and resulting changes to the environment. The effect of a number of important parameters have been investigated, including the bottom slope, wave amplitude, Reynolds number, Richardson number, and Prandtl number. The behavior of oncoming waves when the angle of incidence is near to the critical angle has been the main emphasis. Linear theory is not valid in this range, and recent laboratory studies have focused on different types of internal waves and reflection from relatively steep slopes.

Critical angle reflection is an effective means of dissipating the oncoming wave energy, and, for a broad range of simulations, approximately 90% of the wave energy is dissipated in the boundary layer into heat and mixing of the background density profile. The energetics of the flow show that there is a net negative buoyancy flux for most of the simulations, transferring some wave potential energy into kinetic energy to be dissipated as heat, especially in the viscously dominated region near the wall.

The simulations have shown that the flow behavior and the nature of the turbulence that develop over shallow slopes differ from those for steep slopes. For the steep slope case ($\simeq 30^o$) the flow may be characterized as a turbulent bore, which moves upslope at the phase speed of the oncoming wave. It produces almost continuous, localized mixing that restratifies behind the bore. For the shallower slopes (3^o - 20^o) the turbulence is intermittent and occurs across the breadth of the boundary layer.

The boundary region goes through a mixing cycle approximately once in 1.0 - 1.5 wave periods, where the duration of the cycle is also a function of the bottom slope, increasing in proportion to the wave period as the slope decreases. Between mixing cycles, the boundary

region relaminarizes, restratifies, and sets up a flow field whose most defining feature is a thermal front, which moves upslope at the x-component of the phase speed of the oncoming wave. The observed restratification of the boundary region by buoyancy forces is key to the participation of boundary mixing in contributing to continuous diapycnal mixing in the ocean.

Simulations using different amplitude waves have been useful for examining properties of critical angle reflection. Some flow features (turbulent layer thickness, current speeds) respond to changes in wave amplitude in a roughly linearly fashion, while other flow features (mixing period, mixing efficiency) are less sensitive to its changes for different turbulent experiments.

Wave amplification in the turbulent layer causes strong wall-shear stresses to develop, with approximately two orders of magnitude higher shear rates than contained in the oncoming waves. These strong shear stresses, combined with strong local upwelling flow features near the boundary, can cause resuspension of bottom sediment.

A prominent feature of the energetics is a strongly oscillating buoyancy flux, indicative of strong upslope/downslope flow that occurs twice per wave period. It appears that the upslope flow, generated by the oncoming wave interacting with the presence of the boundary, is responsible for setting up wave overturning in the boundary layer that leads to subsequent wave breakdown into turbulence.

Mixing efficiencies for the simulations have been examined and compared to a new, exact solution for a plane wave. The mixing efficiencies for critical angle reflection are approximately 0.35. It has been argued that the higher values obtained here than for laboratory and field measurements can be attributed to differences in Prandtl, Reynolds, and Richardson numbers. The plane-wave solution developed in Section 3.3 was shown to contain features of the mixing discovered by numerical studies.

The numerical experiments have also been successful in showing the behavior of internal wave reflection away from the critical angle. It was found that, close to critical conditions, the flow behaves in a fashion similar to the critical angle flows, with similar mixing efficiencies

and turbulent layer thicknesses. It was also determined that off-critical reflection lengthens the mixing cycle for shallower slopes and shortens it for steeper slopes. Reflection away from the critical angle develops in different manners. Waves reflecting from slopes steeper than their critical angle exhibit increased dissipation rates and mixing, while waves reflecting from shallower slopes experience greater reflection from the boundary.

The results are in qualitative agreement with related laboratory studies and show similar development of features such as boundary current velocities, flow dynamics, and transition Reynolds numbers. Boundary region profiles for these simulations have shown that δ, the turbulent layer thickness, has a maximum value of approximately $\lambda_z/2$ for large amplitude oncoming waves. The turbulent layer thickness was shown to be nearly a linear function of wave amplitude (as also determined in the laboratory for low Richardson number) for the 20^o slope, but insufficient simulations were performed to permit determining the dependence of δ as a function of slope and Richardson and Reynolds numbers.

Also, it was found that the mixing process extends into the interior stratified fluid and is not restricted to a well-mixed boundary region. A key process in this interior communication is the participation of the internal wave field. The oncoming internal wave acts to pump boundary-mixed fluid into the interior and stratified fluid into the boundary layer. After the mixed fluid is communicated into the stratified regions, the fluid is transported farther into the interior, along constant density surfaces as observed in laboratory experiments of boundary mixing *e.g.,* Hopfinger (1987). Particle and dye studies aided in visualization and tracking of net fluid motions, and indicated that there is significant transport of fluid away from the turbulent layer.

The turbulence in the boundary layer radiates energy back upwards across the path of the oncoming internal waves. Changes to the background density profile and the generation of mean currents occur in regions significantly farther from the wall than the depth of the turbulent layer. A net result is a layering of the interior stratification. This process has important implications regarding the capability of internal wave breakdown near sloping boundaries to make large contributions to the overall vertical mixing in the ocean.

Acknowledgements

This work was supported primarily under U.S. Navy Office of Naval Research (ONR) Contract N00014-90-J-1112. Support was also provided for D.N.S. as a Post-Doctoral researcher by ONR Contract N00014-95-1-0047 through a grant to J.S. Allen and R.A. Holman at Oregon State University. Supercomputer support was obtained from NCSA-UIUC and by the College of Oceanic and Atmospheric Sciences, OSU through a grant to M.R. Abbott from the NASA-EOS program.

References

Batchelor, G. K., *An Introduction to Fluid Dynamics* (Cambridge University Press, Cambridge, 615 pp.)

Cacchione, D., Wunsch, C. 1974: "Experimental study of internal waves over a slope," *J. Fluid Mech.,* **66,** 223-239.

Cacchione, D. A., Southard, J. B. 1974: "Incipient sediment movement by shoaling internal gravity waves," *J. Geophys. Res.,* **79,** 2237-2242.

Cacchione, D. A., Drake, D. E. 1986: "Nepheloid layers and internal waves over continental shelves and slopes," *Geo-Marine Letters,* **6,** 147-152.

Cacchione, D. A., Schwab, W. C., Noble, M., Tate, G., 1988: "Internal tides and sediment movement on Horizon Guyot, Mid-Pacific mountains," *Geo-Marine Letters*, **8,** 11-17.

Cacchione, D. A., Drake, D. E. 1990: "Shelf sediment transport: an overview with applications to the northern California continental shelf, *Sea Volume Nine: Ocean Enginnering Science*, John Wiley and Sons, Inc., New York.

Durran, D. R., Brown, R., Slinn, D. N., Yang, M. J. 1993: "Towards more accurate wave-permeable boundary conditions," *Mon. Weather Rev.,* **121,** 604-620.

Eriksen, C. C. 1982: "Observations of internal wave reflection off sloping bottoms," *J. Geophys. Res.,* **87,** C1, 525- 538.

Eriksen, C. C. 1985: "Implications of ocean bottom reflection for internal wave spectra and mixing," *J. Phys. Ocean.,* **15,** 9, 1145-1156.

Eriksen, C. C. 1997: "Internal wave reflection and mixing at Fieberling Guyot," to appear in *J. Geophys. Res., Oceans*

Fuchs, N. A. 1964: *The Mechanics of Aerosols* (Permagon Press, New York. 408 pp.)

Gilbert, D., Garrett, C. 1989: "Implications for ocean mixing of internal wave scattering off irregular topography," *J. Phys. Ocean.,* **19,** 1716-1729.

Gilbert, D., 1993: "A search for evidence of critical internal wave reflection on the continental rise and slope off Nova Scotia," *Atmosphere-Ocean,* **31,** 99-122.

Gordon, R. L, 1980: "Boundary layer under near-inertial internal waves over a critically sloping bottom," *J. Phys. Ocean.* **10,** 1032-1038.

Holloway, P. E., Barnes, B., 1997: "A numerical investigation into the bottom boundary layer flow and vertical structure of internal waves on a continental slope," submitted to *Continental Shelf Research.*

Hopfinger, E. J. 1987: "Turbulence in stratified fluids: A review," *J. Geophys. Res.,* **92**, 5287-5303.

Huthnance, J. M., 1989: "Internal tides and waves near the continental shelf edge, *Geophys. Astrophys. Fluid Dyn.,* **48** 81-106.

Itsweire, E. C., Helland, K. N., Van Atta, C. W. 1986: "The evolution of grid-generated turbulence in a stably stratified fluid," *J. Fluid Mech.,* **162,** 299-338.

Ivey, G. N., Nokes, R. I. 1989: "Vertical mixing due to the breaking of critical internal waves on sloping boundaries," *J. Fluid Mech.*, **204,** 479-500.

Ledwell, J. R., Hickey, B. M., 1995: "Evidence for enhanced boundary mixing in the Santa Monica basin," *J. Geophys. Res.* **100,** 20665-20679.

Lele, S. K. 1992: "Compact finite difference schemes with spectral-like resolution," *J. Comp. Physics,* **103,** 16-42.

Petruncio, E. T., Rosenfeld, L. K., Paduan, J. D., 1997: "Observations of the internal tide in Monterey Submarine Canyon," submitted to *J. Phys. Ocean.*

Phillips, O. M., 1970: "On flows induced by diffusion in a stably stratified fluid," *Deep-Sea Res.,* **17,** 435-443.

Phillips, O. M., 1977: *The Dynamics of the Upper Ocean,* 2nd ed. (Cambridge University Press, New York, 336 pp.)

Rehmann, C. R., Koseff, J. R. 1994: "Mixing efficiency of decaying grid turbulence in a stratified fluid," Fourth International Symposium on Stratified Flow, Institute de Mecanique, Grenoble, France.

Rohr, J., Van Atta, C. 1987: "Mixing efficiency in stabley stratified growing turbulence," *J. Geopys. Res.,* **92,** 5481-5488.

Slinn, D. N., 1995: *Numerical simulation of turbulent mixing caused by internal wave reflection from sloping boundaries,* Ph.D. Dissertation, University of Washington, 398 pp.

Slinn, D. N., Riley, J. J., 1996: "Turbulent mixing in the oceanic boundary layer caused by internal wave reflection from sloping terrain," *Dynamics of Atmospheres and Oceans,* **24,** 51-62.

Slinn, D. N., Riley, J. J., 1997a. "Turbulent dynamics of a critically reflecting internal gravity wave," submitted to *Theoretical and Computational Fluid Dynamics.*

Slinn, D. N., Riley, J. J., 1997b. "A model for the simulation of turbulent boundary layers in an incompressible stratified flow," submitted to *J. Computational Physics.*

Southard, J. B., Cacchione, D. A. 1972: "Experiments on bottom sediment movement by breaking internal waves," in *Shelf Sediment Transport,* (Edited by Swift, Duane, and Pilkey; Dowden, Hutchinson, and Ross, Inc. Stroudsburg, Pa.) 83-97.

Stillinger, D. C., Helland, K. N., Van Atta, C. W. 1983: "Experiments on the transition of homogenoeus turbulence to internal waves in a stratified fluid, *J. Fluid Mech.,* **131,** 91-122.

Taylor, J. R. 1993: "Turbulence and mixing in the boundary layer generated by shoaling internal waves," *Dynamics of Atmos. and Oceans,* **19,** 233-258.

Thorpe, S. A. 1987: "Current and temperature variability on the continental slope," *Phil. Trans. R. Soc. London.,* A, **323,** 471-517.

Thorpe, S. A., Haines, A. P. 1987: "On the reflection of a train of finite-amplitude internal waves from a uniform slope," *J. Fluid Mech.,* **178,** 279-302.

Thorpe, S. A. 1989: "The distortion of short internal waves produced by a long wave, with application to ocean boundary mixing," *J. Fluid Mech.*, **208,** 395-415.

Thorpe, S. A., Hall, P., and Wite, M. 1990: "The variablity of mixing on a continental slope," *Proc. Royal Soc.,* **A439**, 115-130.

Thorpe, S. A. 1992: "Thermal fronts caused by internal gravity waves reflecting from a slope," *J. Phys. Ocean.,* 22, 105-108.

Toole, J. M., Polzin, K. L., and Schmidt, R. W., 1994: "Estimates of diapycnal mixing in the abyssal ocean," *Science*, **264**, 1120-1123.

White, M., 1994: "Tidal and subtidal variability in the sloping benthic boundary layer," *J. Geophys. Res.* **99,** 7851-7864.

Winters, K. B. 1989: *Intensification and instability of internal gravity waves at caustics and critical levels,* Ph.D. Thesis, University of Washington, 194 pp.

Winters, K. B., Lombard, P. N., Riley, J. J., D'Asaro, E. A. 1995: "Available potential energy and mixing in density stratified fluids," *J. Fluid Mechanics,* **289,** 115-128.

Wolanski, E., 1987: "Some evidence for boundary mixing near coral reefs," *Limnol. Oceanogr.,* **32,** 735-739.

Wunsch, C., Hendry, R., 1972: "Array measurements of the bottom boundary layer and the internal wave field on the continental slope," *Geophys. Fluid Dynamics,* **4,** 101-145.

Table 1: Critical Angle Simulations

Case	α	Re	Ri	ω	Classification
1	3.4	620	131	0.06	laminar
2	3.4	830	72	0.06	laminar
3	3.4	2100	44	0.06	turbulent
4	3.4	2600	29	0.06	turbulent
5	5.0	1860	59	0.09	transition
6	5.0	2400	36	0.09	turbulent
7	5.0	3300	33	0.09	turbulent
8	7.7	750	125	0.13	laminar
9	7.7	1500	130	0.13	turbulent
10	7.7	3000	135	0.13	turbulent
11	9.2	850	61	0.16	laminar
12	9.2	1200	53	0.16	transition
13	9.2	2000	43	0.16	turbulent
14	9.2	2800	40	0.16	turbulent
15	9.2	3600	46	0.16	turbulent
16	9.2	3600	46	0.16	$Pr = 0.6$
17	9.2	3600	46	0.16	$Pr = 2.0$
18	20.0	425	1700	0.34	laminar
19	20.0	540	125	0.34	laminar
20	20.0	800	120	0.34	transition
21	20.0	850	430	0.34	transition
22	20.0	1100	110	0.34	turbulent
23	20.0	1200	235	0.34	turbulent
24	20.0	1800	92	0.34	turbulent
25	20.0	1800	92	0.34	$2\lambda_y$
26	20.0	1800	92	0.34	$2\lambda_x$
27	20.0	2400	53	0.34	turbulent
28	30.0	450	490	0.50	laminar
29	30.0	570	150	0.50	turbulent
30	30.0	800	625	0.50	turbulent
31	30.0	800	156	0.50	turbulent
32	30.0	1000	108	0.50	$2\lambda_x$
33	30.0	1370	120	0.50	$2\lambda_x$
34	30.0	1700	138	0.50	turbulent

Table 2: Energy Budgets at Critical Angle

Case	Slope	Reynolds No.	Mixing	Heat	Radiate
1	3.4	620	0.33	0.62	0.05
2	3.4	830	0.35	0.55	0.10
3	3.4	2100	0.39	0.54	0.07
4	3.4	2600	0.39	0.48	0.13
5	5.0	1860	0.38	0.60	0.02
6	5.0	2400	0.39	0.52	0.09
7	5.0	3300	0.37	0.50	0.13
8	7.7	750	0.37	0.61	0.02
9	7.7	1500	0.33	0.55	0.12
10	7.7	3000	0.35	0.57	0.08
11	9.2	850	0.36	0.58	0.06
12	9.2	1200	0.38	0.50	0.12
13	9.2	2000	0.36	0.45	0.19
14	9.2	2800	0.37	0.48	0.15
15	9.2	3600	0.32	0.56	0.12
16	9.2	3600	0.38	0.50	0.12
17	9.2	3600	0.27	0.62	0.11
18	20.0	425	0.32	0.67	0.01
19	20.0	540	0.37	0.60	0.03
20	20.0	800	0.36	0.57	0.07
21	20.0	850	0.36	0.62	0.02
22	20.0	1100	0.35	0.54	0.11
23	20.0	1200	0.36	0.61	0.03
24	20.0	1800	0.34	0.53	0.13
25	20.0	1800	0.34	0.54	0.12
26	20.0	1800	0.35	0.53	0.12
27	20.0	2400	0.35	0.50	0.15
28	30.0	450	0.34	0.66	0.00
29	30.0	570	0.40	0.59	0.01
30	30.0	800	0.32	0.66	0.02
31	30.0	800	0.37	0.58	0.05
32	30.0	1000	0.39	0.60	0.01
33	30.0	1370	0.38	0.57	0.05
34	30.0	1700	0.37	0.61	0.02

Table 3: Off Critical Angle Simulations

Case	α	Re	Ri	A_r/A_i	U_M/U	Classification
35	0.0	620	235	1.0	1.5	laminar
36	0.0	1250	59	1.0	1.6	laminar
37	5.0	1100	170	3.3	2.50	laminar
38	5.0	1900	94	3.3	2.56	transition
39	5.0	2300	64	3.3	2.29	turbulent
40	8.0	1500	37	13.9	2.30	turbulent
41	9.2	850	61	∞	1.53	laminar
42	9.2	1200	53	∞	1.78	transition
43	9.2	2000	40	∞	1.95	turbulent
44	9.2	2800	40	∞	2.29	turbulent
45	9.2	3600	46	∞	2.44	turbulent
46	10.5	950	84	15.1	2.22	transition
47	10.5	2470	77	15.1	2.47	turbulent
48	10.5	3690	35	15.1	2.36	turbulent
49	13.5	970	74	5.2	2.00	laminar
50	13.5	2120	62	5.2	2.44	turbulent

Table 4: Energy Budgets Off Critical Angle

Case	α	Re	Mixing	Heat	Radiate
35	0.0	620	0.30	0.37	0.33
36	0.0	1250	0.33	0.41	0.25
37	5.0	1100	0.29	0.44	0.27
38	5.0	1900	0.33	0.42	0.25
39	5.0	2300	0.37	0.45	0.18
40	8.0	1500	0.38	0.46	0.16
41	9.2	850	0.36	0.58	0.06
42	9.2	1200	0.38	0.50	0.12
43	9.2	2000	0.36	0.45	0.19
44	9.2	2800	0.37	0.48	0.15
45	9.2	3600	0.32	0.56	0.12
46	10.5	950	0.35	0.46	0.19
47	10.5	2470	0.34	0.56	0.10
48	10.5	3690	0.40	0.45	0.15
49	13.5	970	0.34	0.58	0.08
50	13.5	2120	0.36	0.58	0.06

Table 5: Mixing Periods for Off Critical Angle Simulations

α	0.0	5.0	8.0	9.2	10.5	13.5
T_M	∞	100	60	48	42	34
T_{W_c}	∞	72	45	39	35	28
$\frac{T_M}{T_{W_c}}$		1.39	1.33	1.23	1.2	1.21

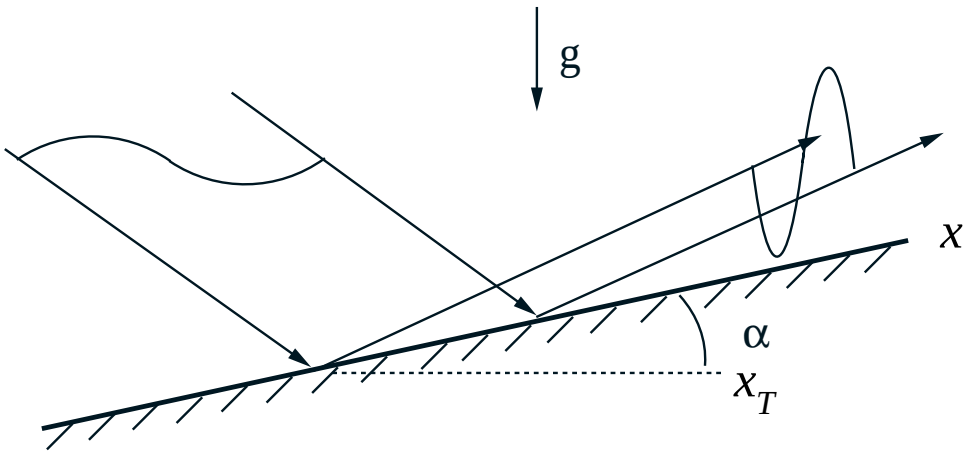

Figure 1: Ray tube reflection diagram for internal gravity waves reflecting from a sloping boundary.

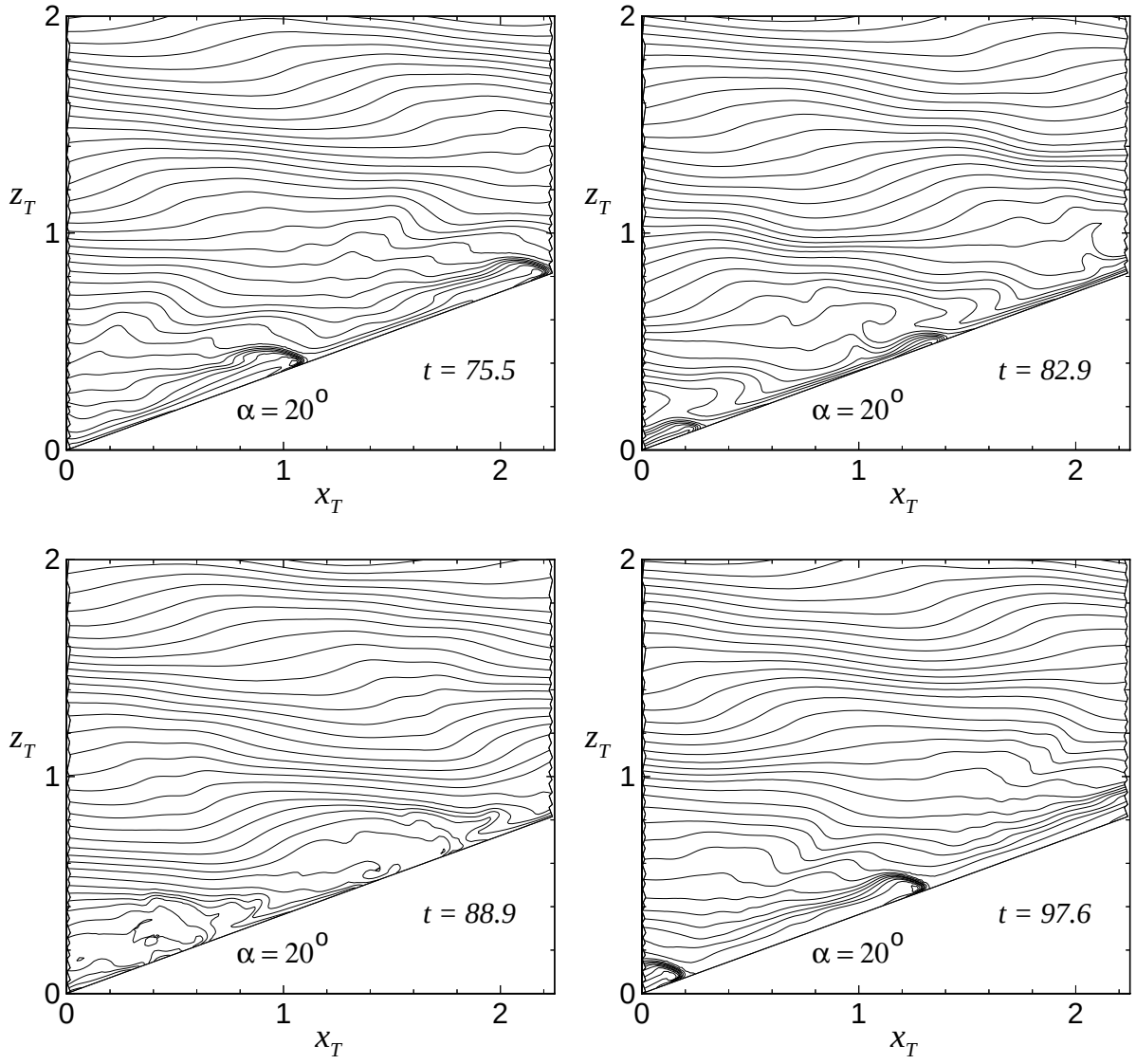

Figure 2: For a bottom slope of 20^o (Case 26), isopycnals of the flow in the near wall region at $t = 75.5$, 82.9, 88.9, and 97.6. In this and all of the subsequent figures the horizontal and vertical axes x_T and z_T are nondimensionalized by λ_z.

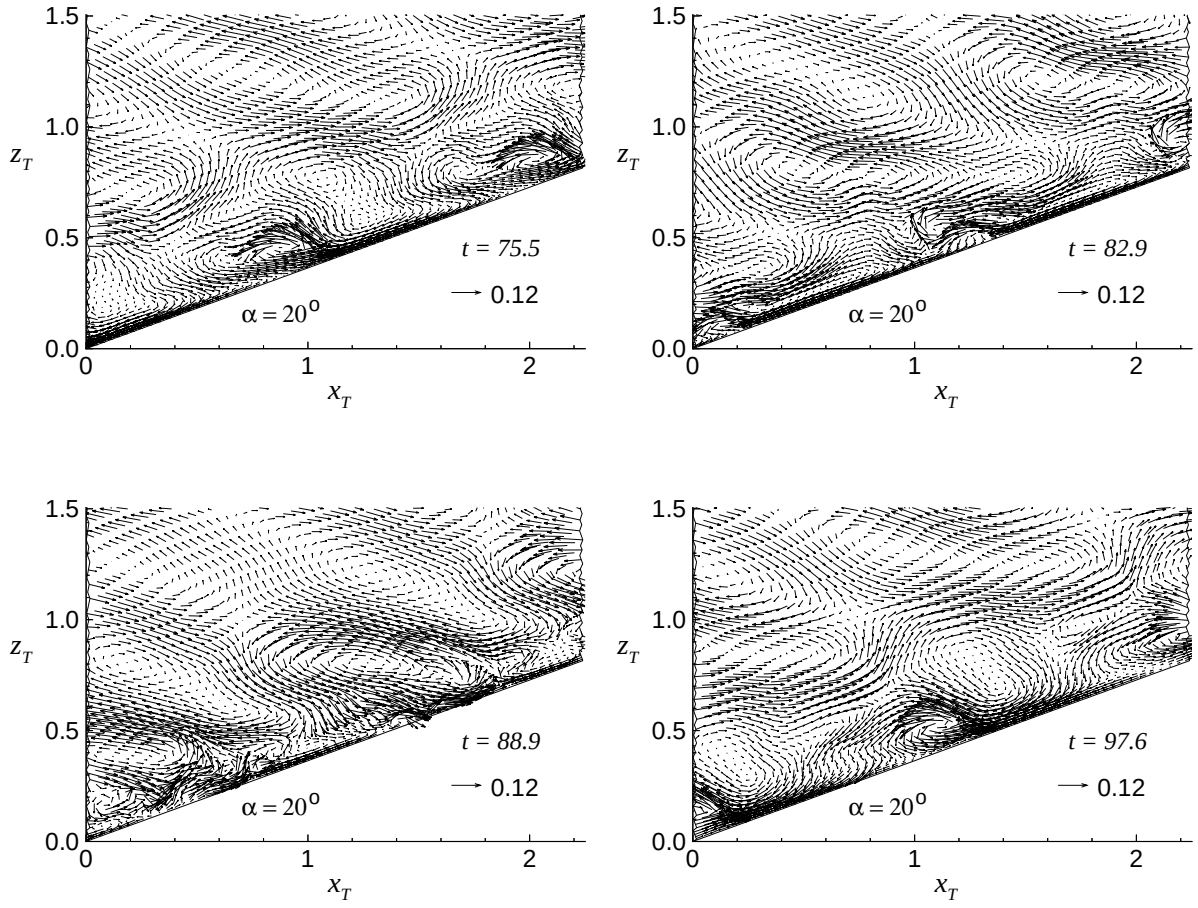

Figure 3: Velocity vectors corresponding to the same sequence as Figure 2 are shown throughout a mixing cycle at $t = 75.5$, 82.9, 88.9, and 97.6, for a bottom slope of 20^o (Case 26).

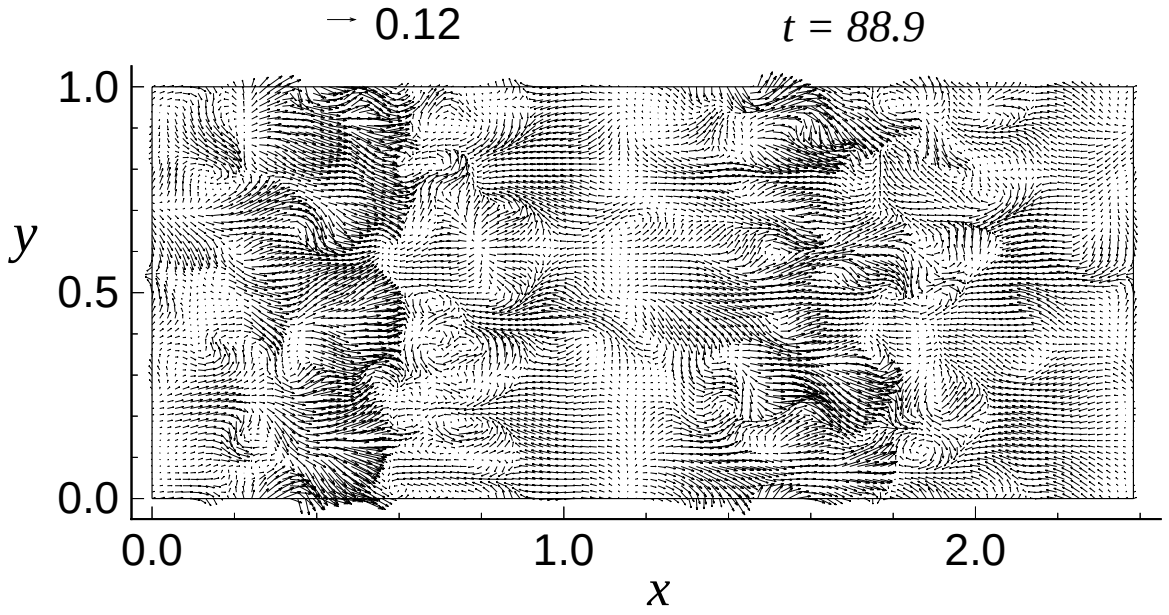

Figure 4: Velocity vectors in a x-y plane parallel to the bottom slope at a height $z = 0.137\lambda_z$ at $t = 88.9$ for Case 26.

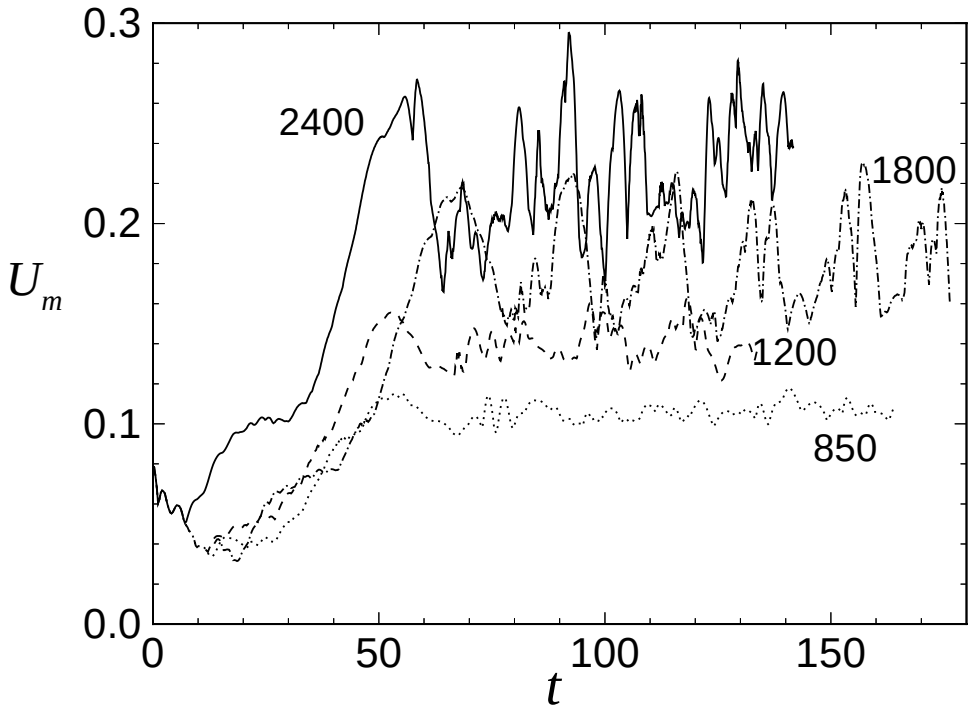

Figure 5: The maximum velocities in the boundary layer for four experiments at different Reynolds numbers (850, 1200, 1800, and 2400) and corresponding wave amplitudes A/A_o (0.3, 0.45, 0.6, $0.8A_o$) over a 20^o bottom slope.

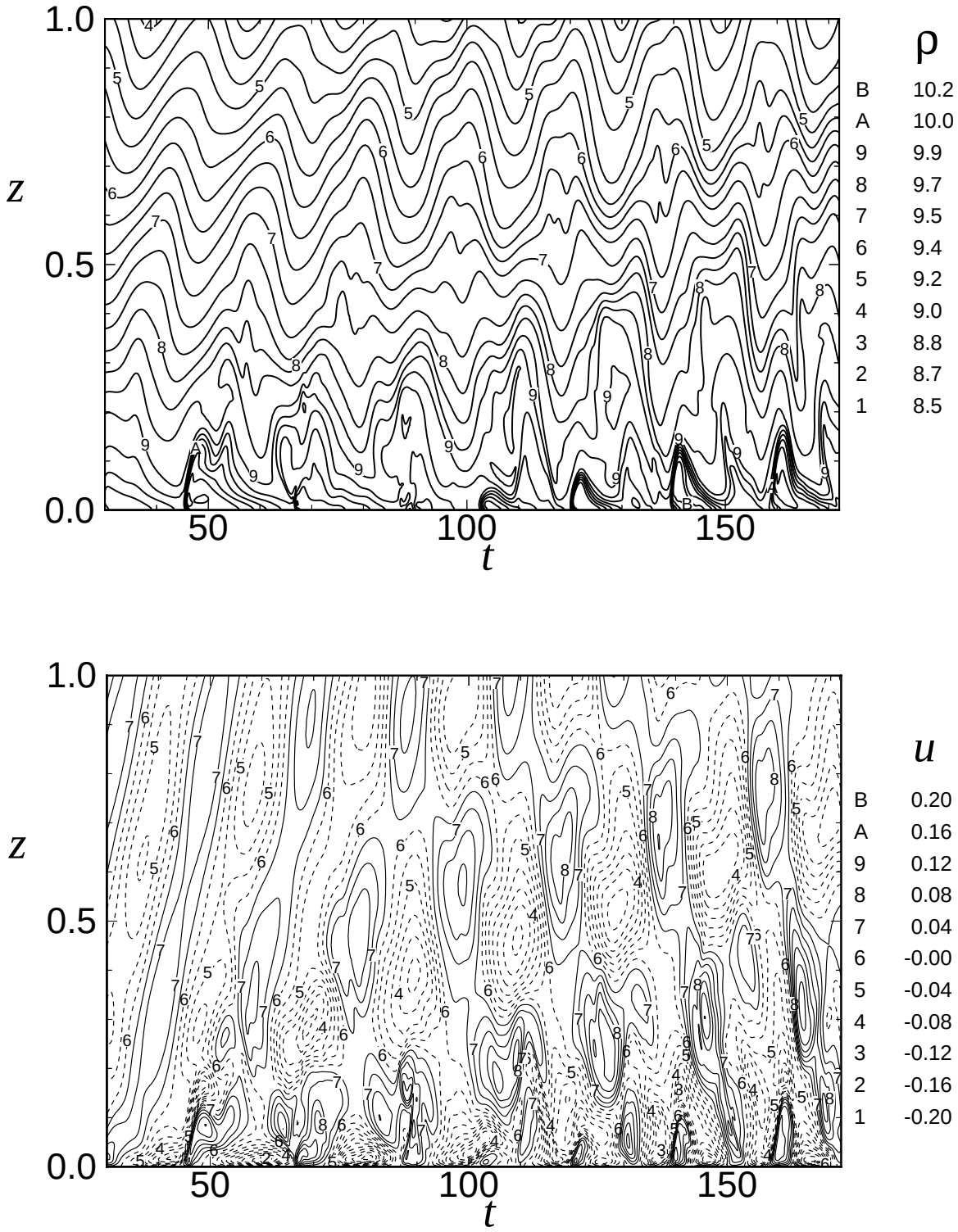

Figure 6: Density field measurements (top) taken along a line perpendicular to the slope from $t = 30$ to $t = 172$ throughout 7.7 wave periods for Case 26 and the u-velocity (bottom) at the same location as a function of time (solid lines, upslope, dashed lines, downslope.)

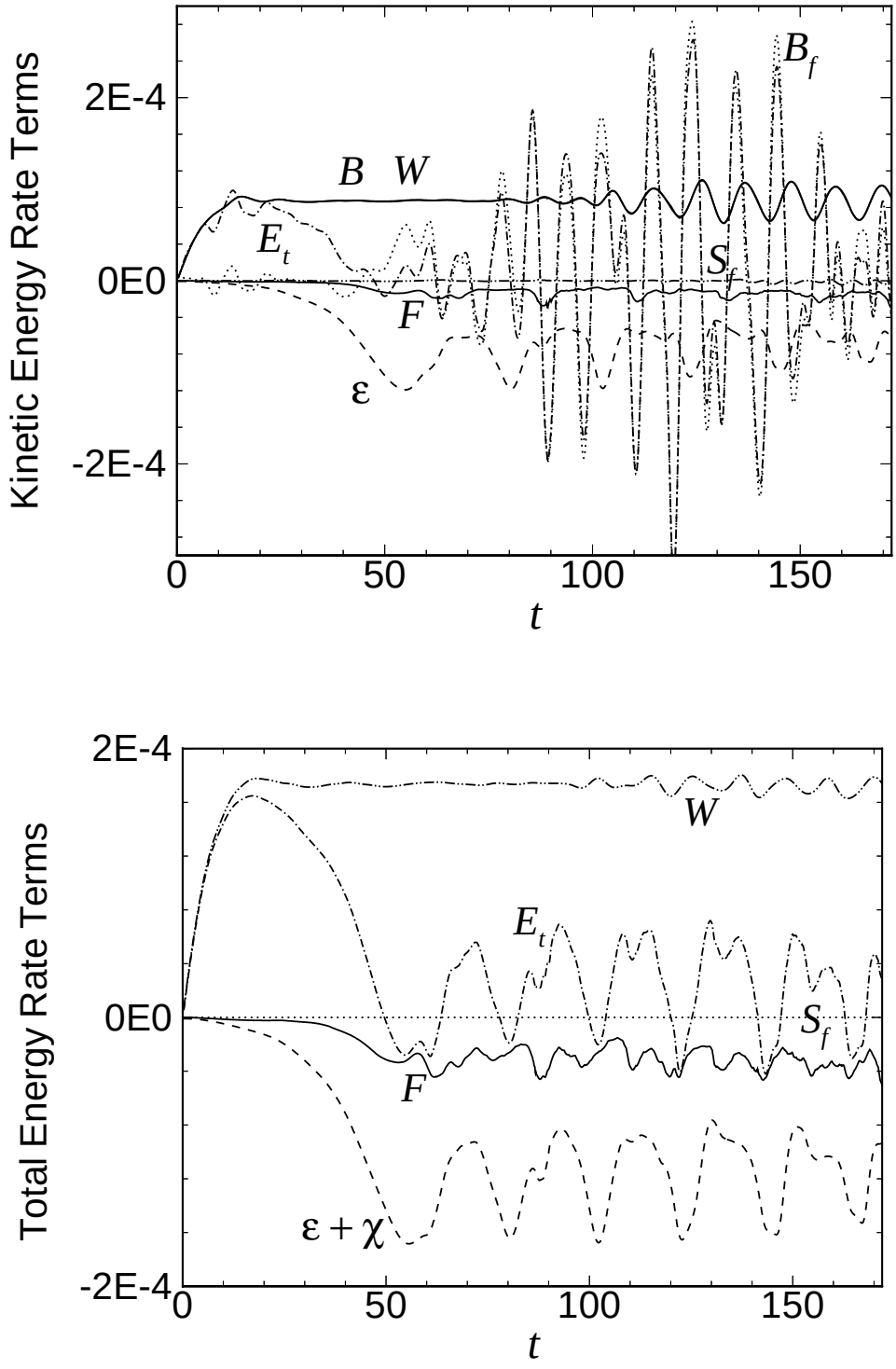

Figure 7: Evolution of terms in the kinetic energy equation (2.12) (top) and the total energy equation (2.12 + 2.13) (bottom) plotted for 20^o slope: work input $\overline{W_{KE}}$ and $\overline{W_{TE}}$, balance of energy term $\overline{B_{KE}}$, change in energy in time $\overline{E_{KEt}}$ and $\overline{E_{TEt}}$, dissipation rates $\overline{\epsilon}$ and $\overline{\chi}$, filter dissipation rates $\overline{F_{KE}}$ and $\overline{F_{TE}}$, buoyancy flux $\overline{B_f}$, and flux of energy into sponge layer $\overline{S_{fKE}}$ and $\overline{S_{fTE}}$.

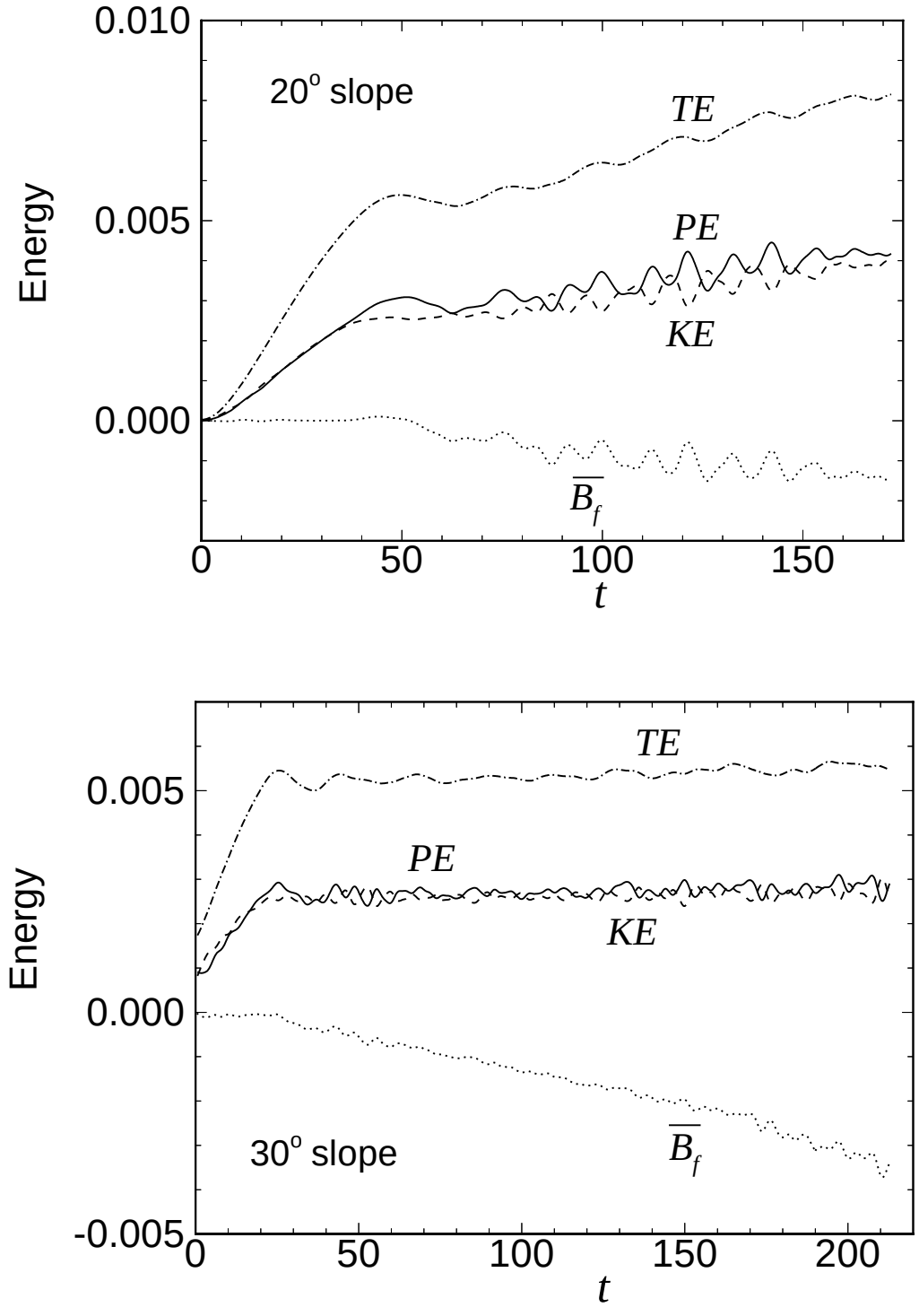

Figure 8: Volume integrals of kinetic, potential, and total energy and the time integrated buoyancy flux $\overline{B_f}$ for critical angle experiments Case 26, 20^o slope (top) and Case 34, 30^o slope (bottom).

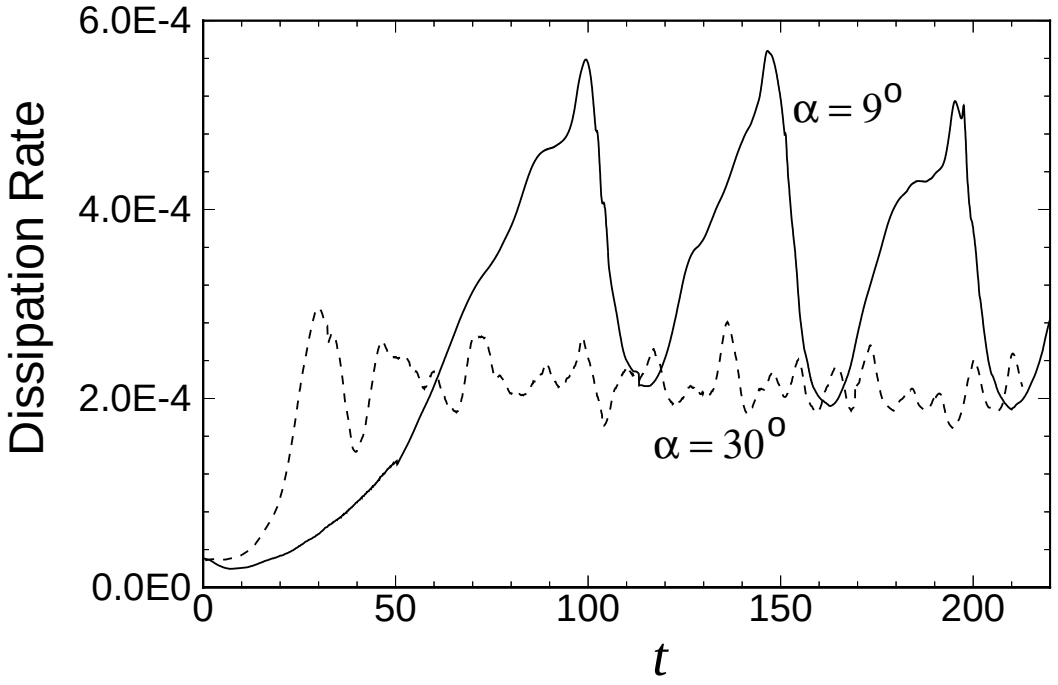

Figure 9: Evolution of dissipation rates for slopes of 9^o (Case 15) and 30^o (Case 34).

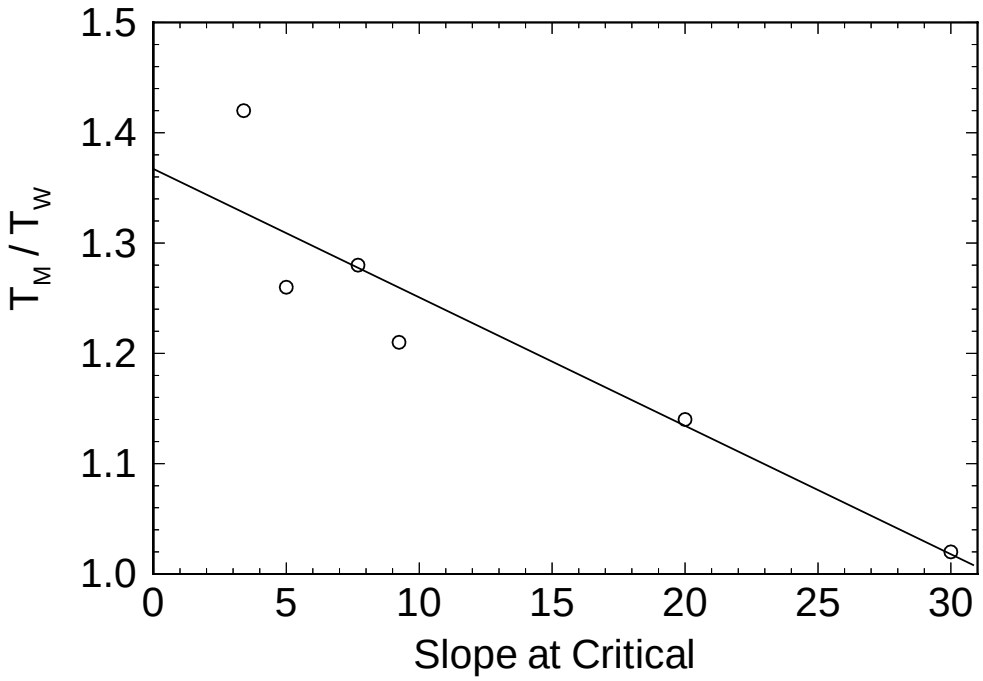

Figure 10: The average ratio of the mixing period to the wave period for critical angle simulations between 3^o and 30^o.

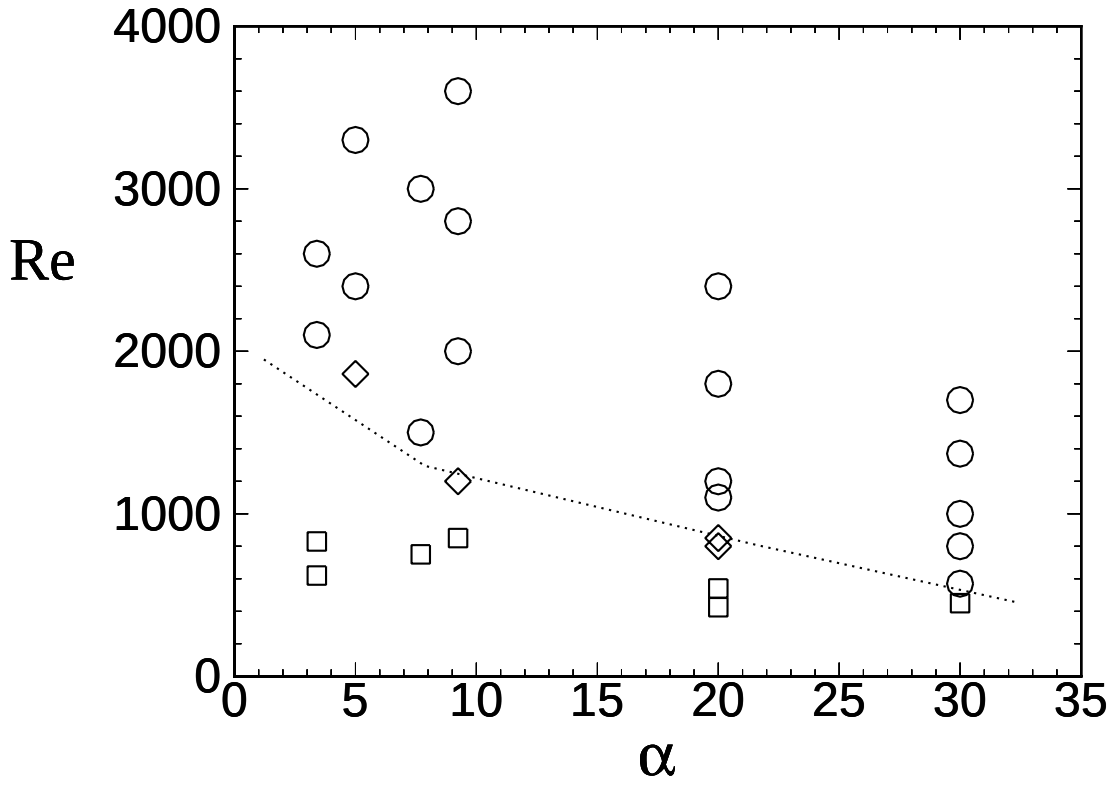

Figure 11: Simulations located on ranges of Reynolds number and slope. Turbulent simulations are located with circles; laminar simulations with squares; and approximate transitional simulations with diamonds. The dashed line indicates the approximate transition Reynolds numbers.

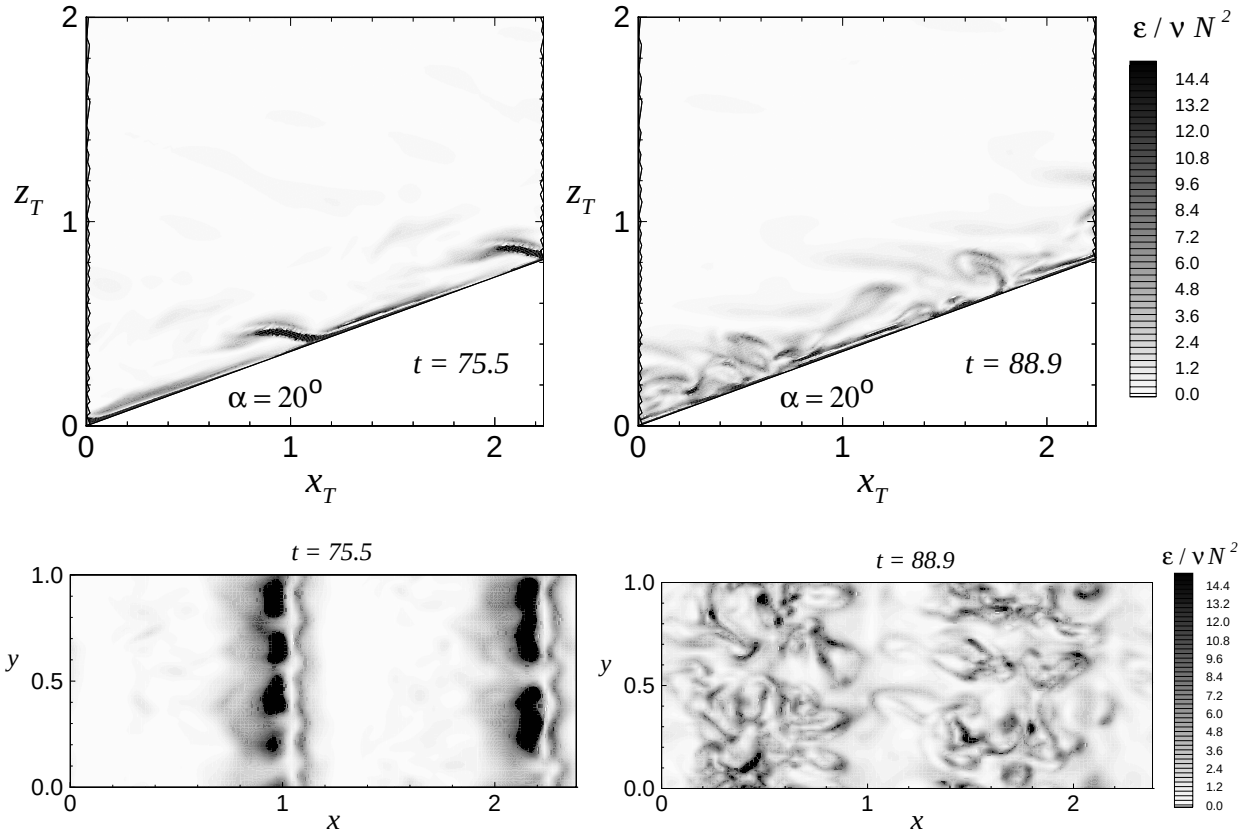

Figure 12: Dissipation Reynolds number, $Re_d = \epsilon/\nu N^2$, for a bottom slope of 20^o (Case 26) at $t = 75.5$ and 88.9. The top frames are side views (x-z planes) located at $y = 0.5$, and the bottom frames are a top view (x-y planes) located at $z = 0.14\lambda_z$.

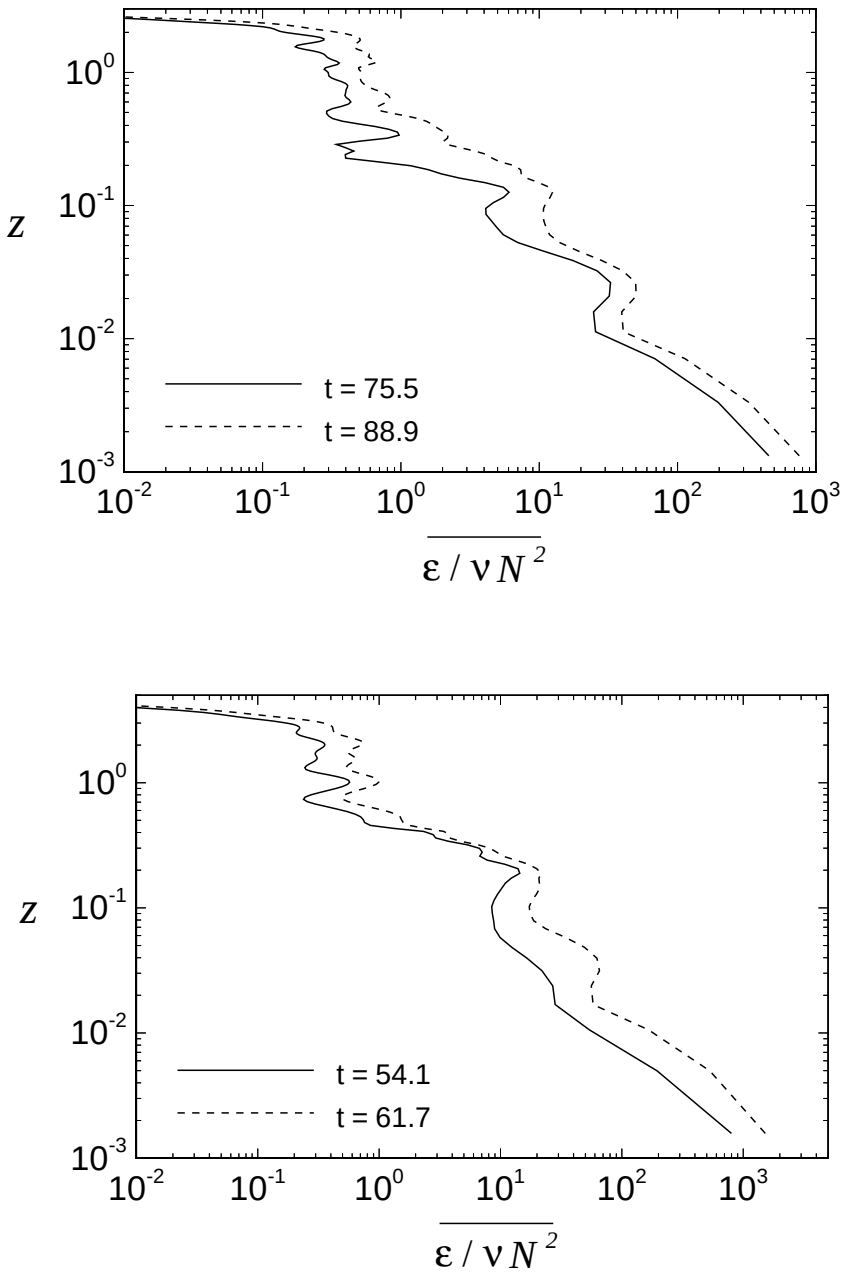

Figure 13: The horizontally averaged dissipation Reynolds number, Re_d, as a function of height from the boundary for 20^o slope (Case 26) at $t = 75.5$ and 88.9 (top) and the 30^o slope (Case 34) at $t = 54.1$ and 61.7 (bottom).

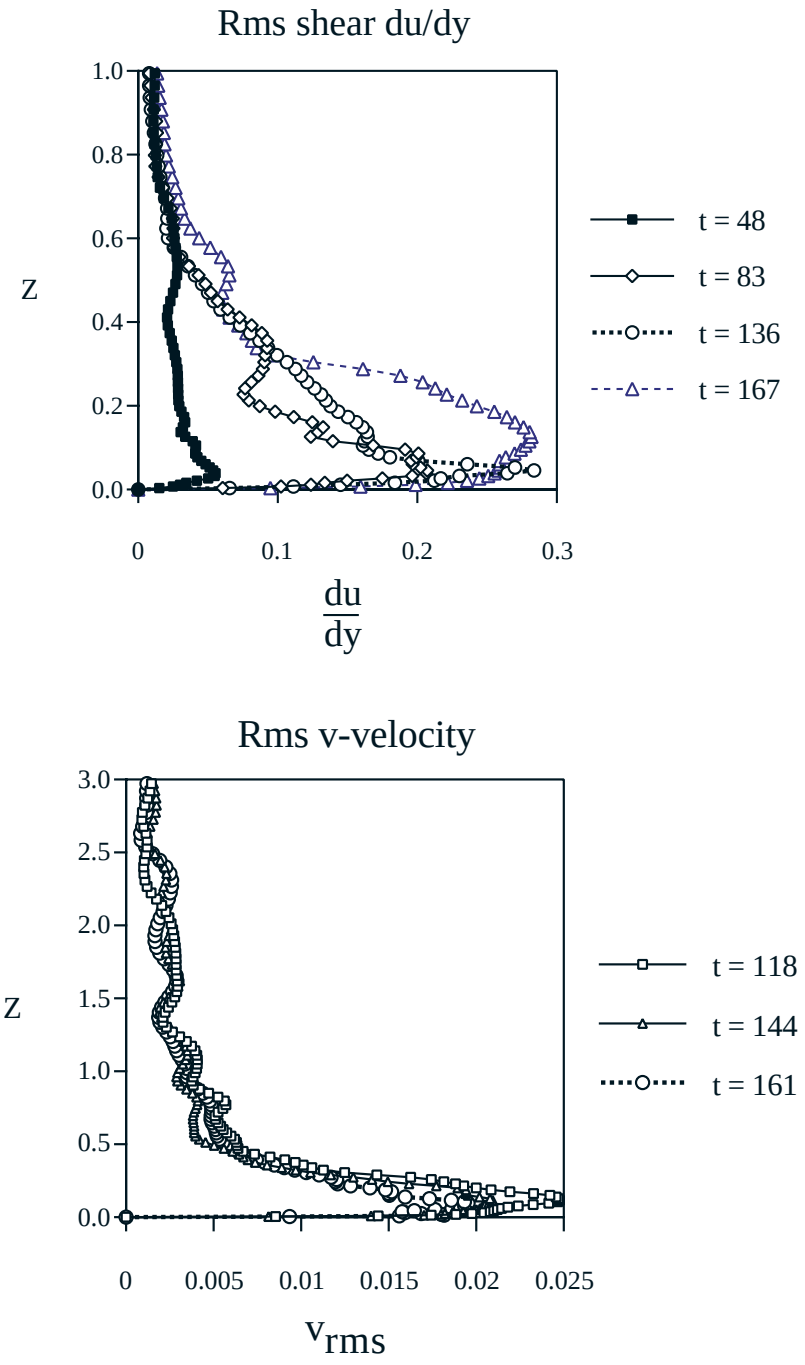

Figure 14: The horizontally integrated rms intensity of $\partial u/\partial y$ at $t = 48$, 83, 136, and 167 for the 20^o slope of Case 24 (top). The rms v-velocity as a function of z for Case 34 (30^o slope) at $t = 118$, 144, and 161 (bottom).

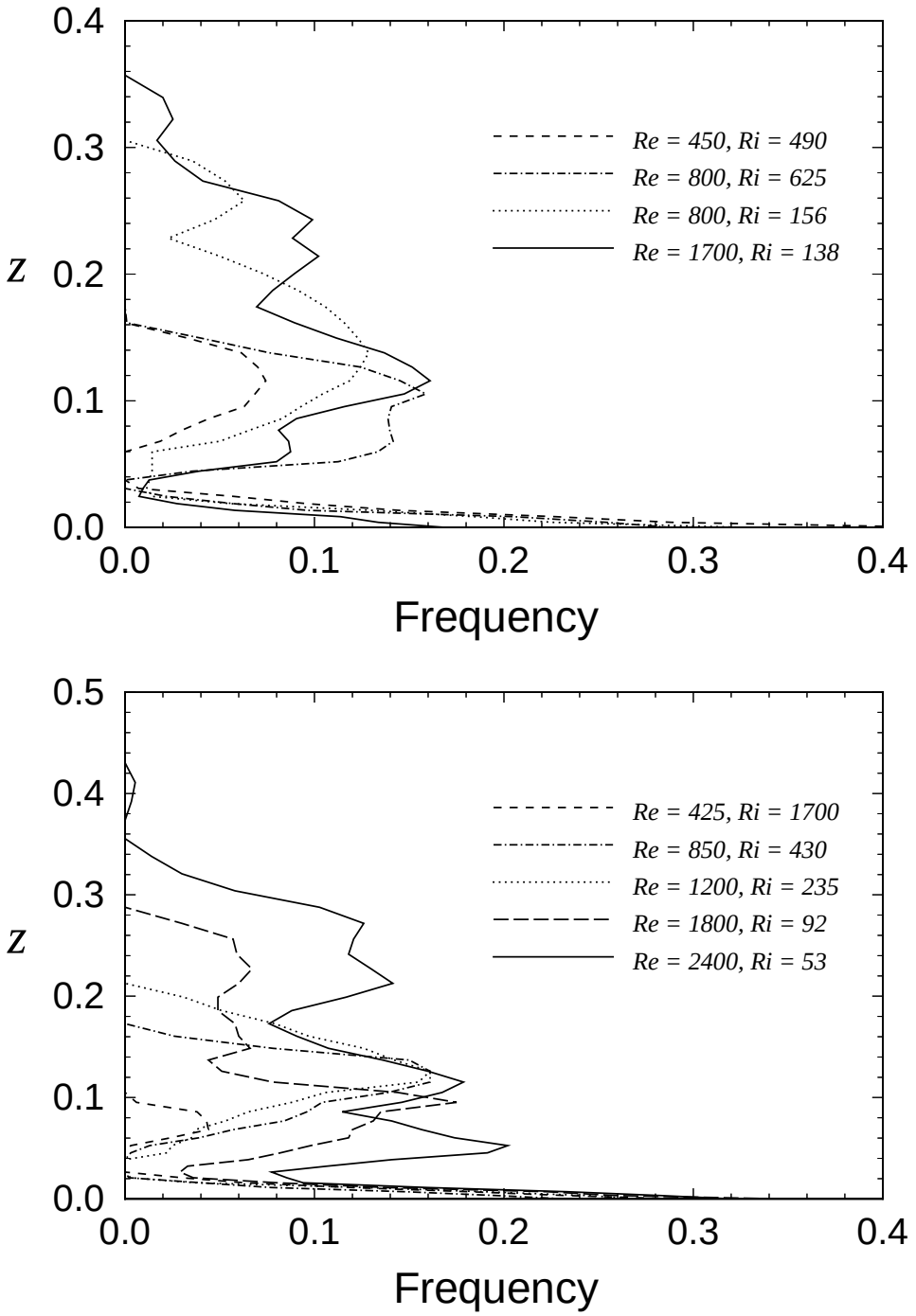

Figure 15: The statistical frequency of statically unstable fluid as a function of height for experiments over a 30^o bottom slope: for Case 28, $Re = 450$; Case 30, $Re = 800$; Case 31, $Re = 800$; and Case 34, $Re = 1700$ (top); and for experiments over a 20^o bottom slope: Case 18, $Re = 425$; Case 21, $Re = 850$; Case 23, $Re = 1200$; Case 26, $Re = 1800$; Case 27, $Re = 2400$ (bottom).

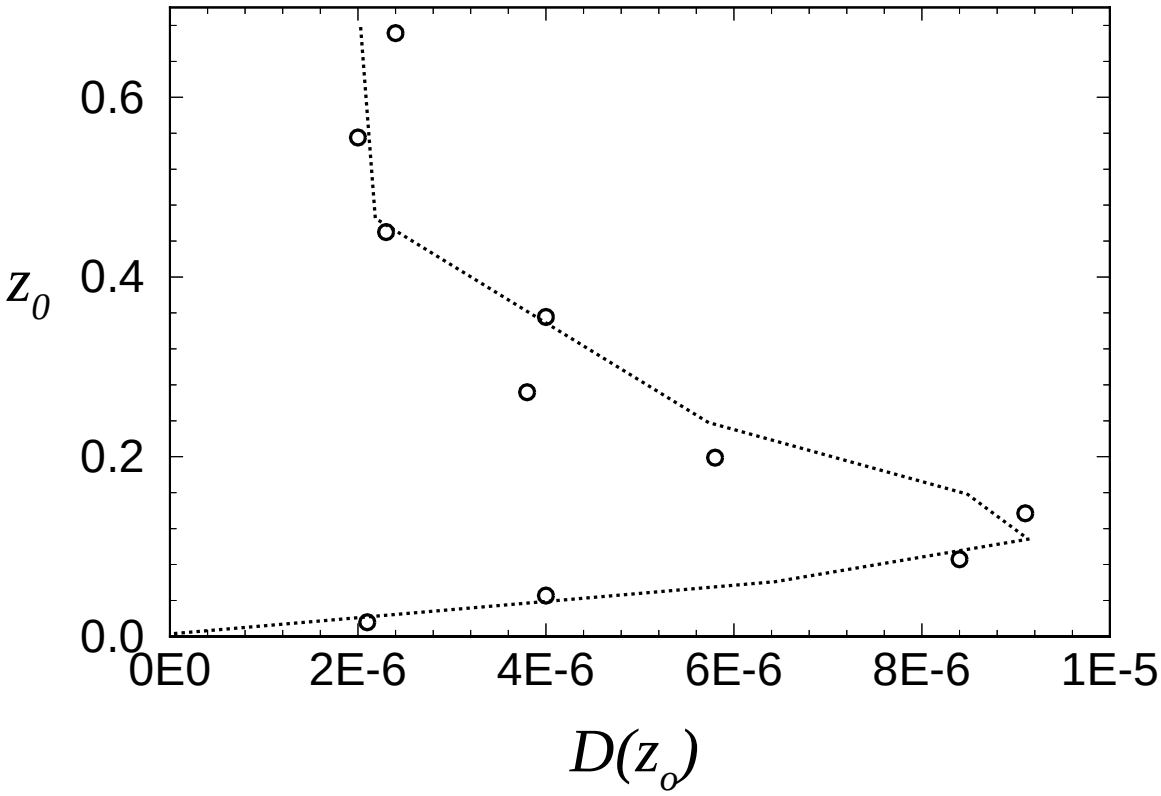

Figure 16: Vertical diffusion coefficients $D(z_0)$ as a function of height of initial release determined from particle dispersion. The dashed line sketchs the approximate z dependence.

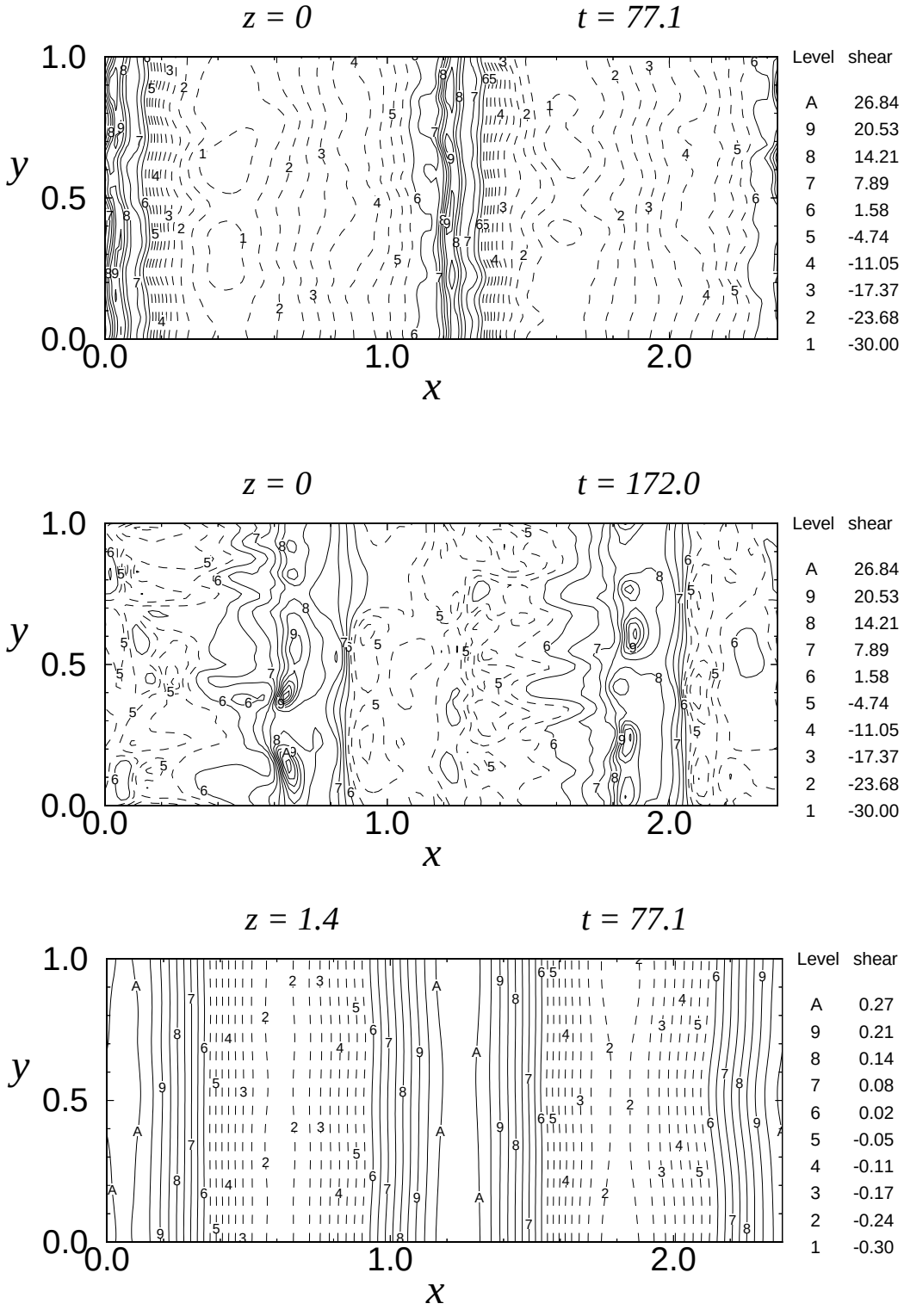

Figure 17: Shear rate contours of $\partial u/\partial z$ at the bottom boundary ($z = 0$) at $t = 77.1$ and 133.7 and at $z = 1.1$ at 133.7 for Case 26.

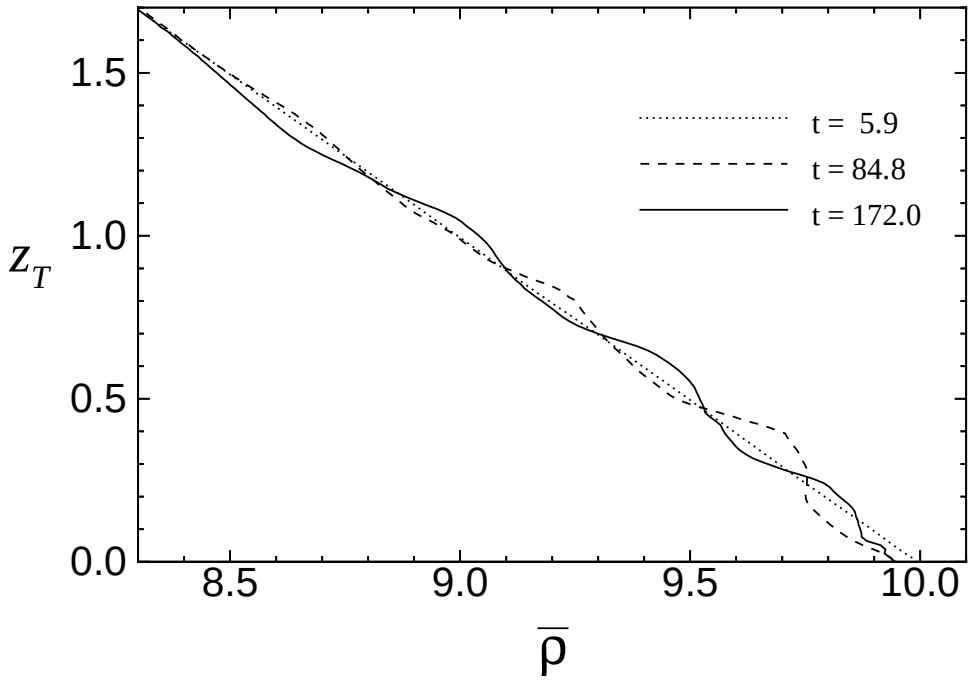

Figure 18: Horizontally averaged density profiles as a function of height for the 20^o bottom slope (Case 26) at $t = 5.9$, 84.8, and 172.

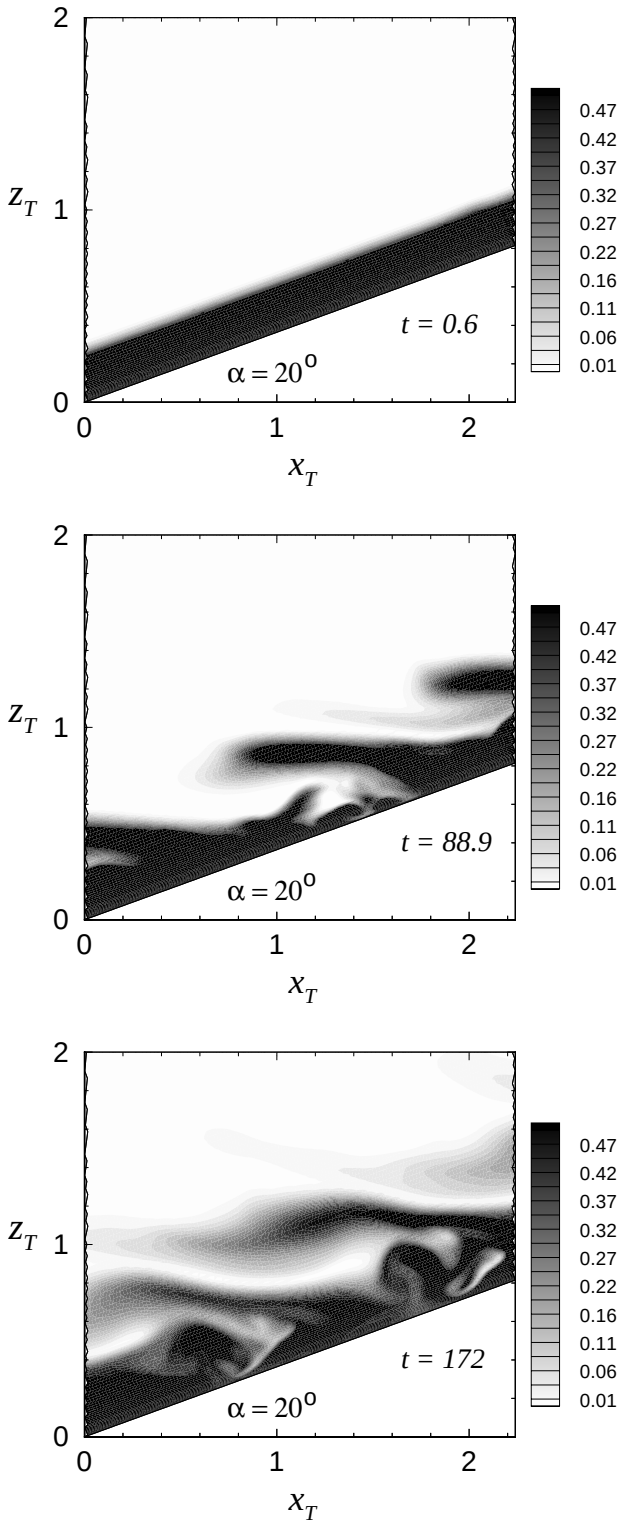

Figure 19: Dye fields for Case 26 for a 20^o bottom slope at $t = 0.6$, 88.9, and 172.

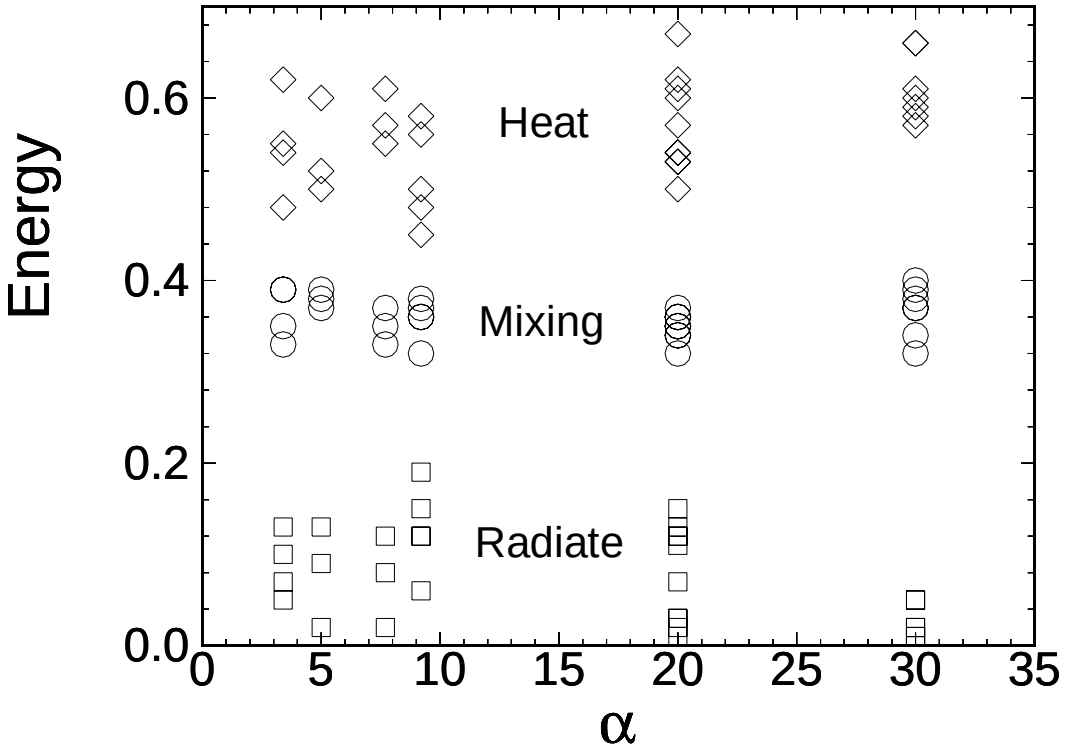

Figure 20: Mixing efficiencies (circles), heat gain coefficients (diamonds), and radiation coefficients (squares) for the critical angle simulations as a function of bottom slopes.

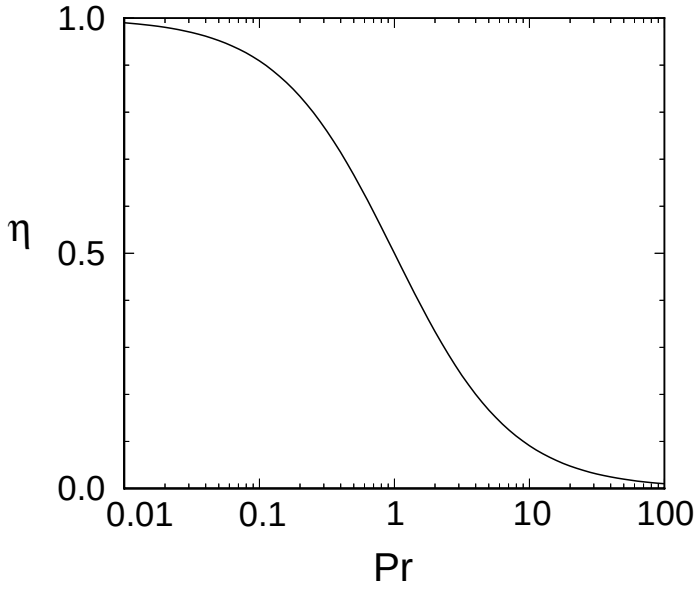

Figure 21: The mixing efficiency for viscously decaying plane internal waves, defined here as $\eta_2 = \overline{\chi}/(\overline{\chi} + \overline{\epsilon})$, as a function of Prandtl number.

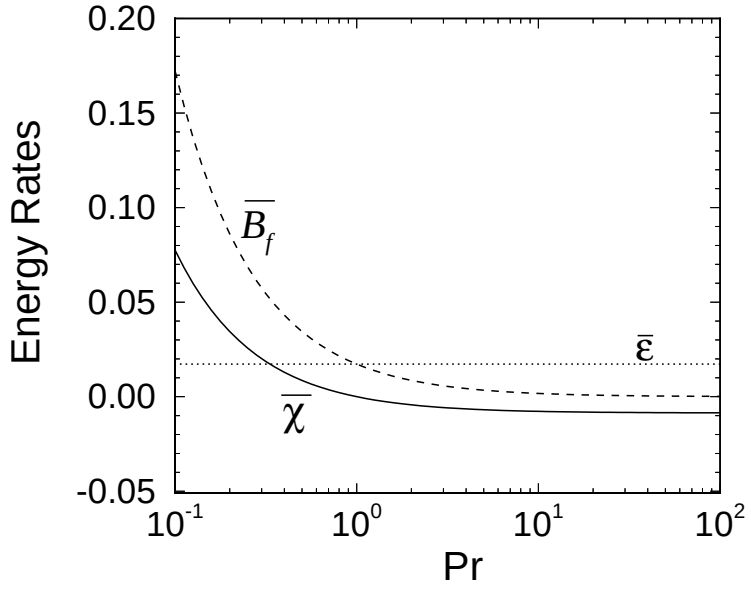

Figure 22: The average buoyancy flux ($\overline{B_f}$), $\overline{\epsilon}$, and $\overline{\chi}$ as a function of Prandtl number for a plane internal gravity wave at $Re = 1000$.

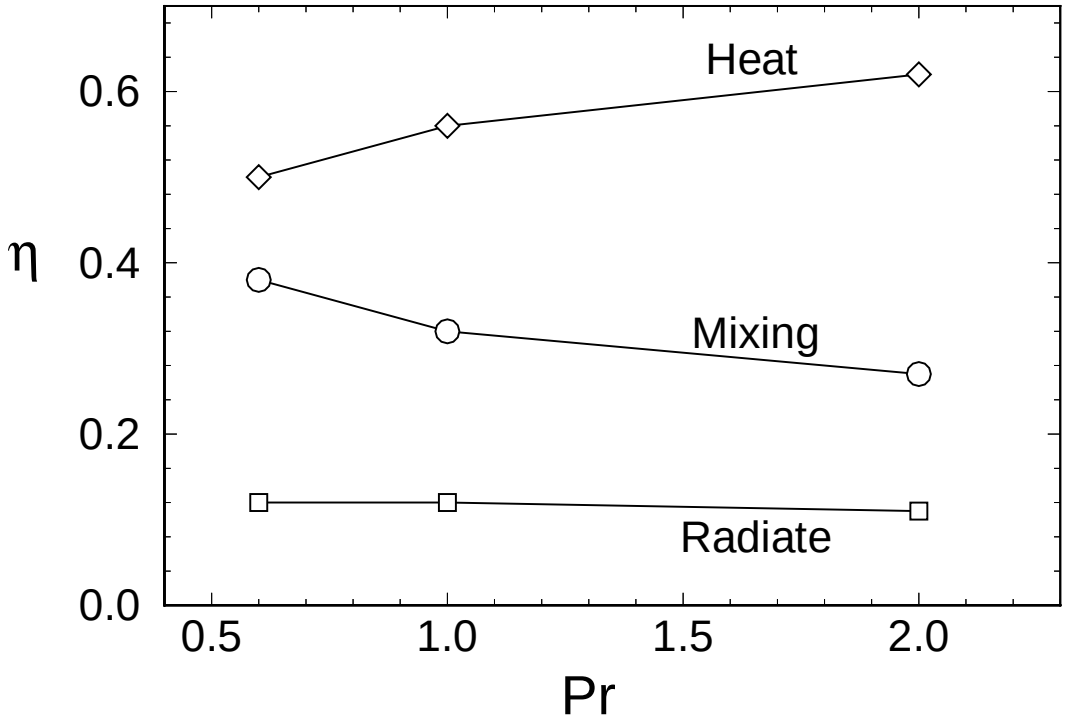

Figure 23: Values of mixing efficiency (circles), heat gain (diamonds), and energy radiated from the boundary layer region (squares) for critical angle experiments over a 9.2^o slope at $Re = 3600$ and Prandtl numbers of 0.6, 1.0, and 2.0.

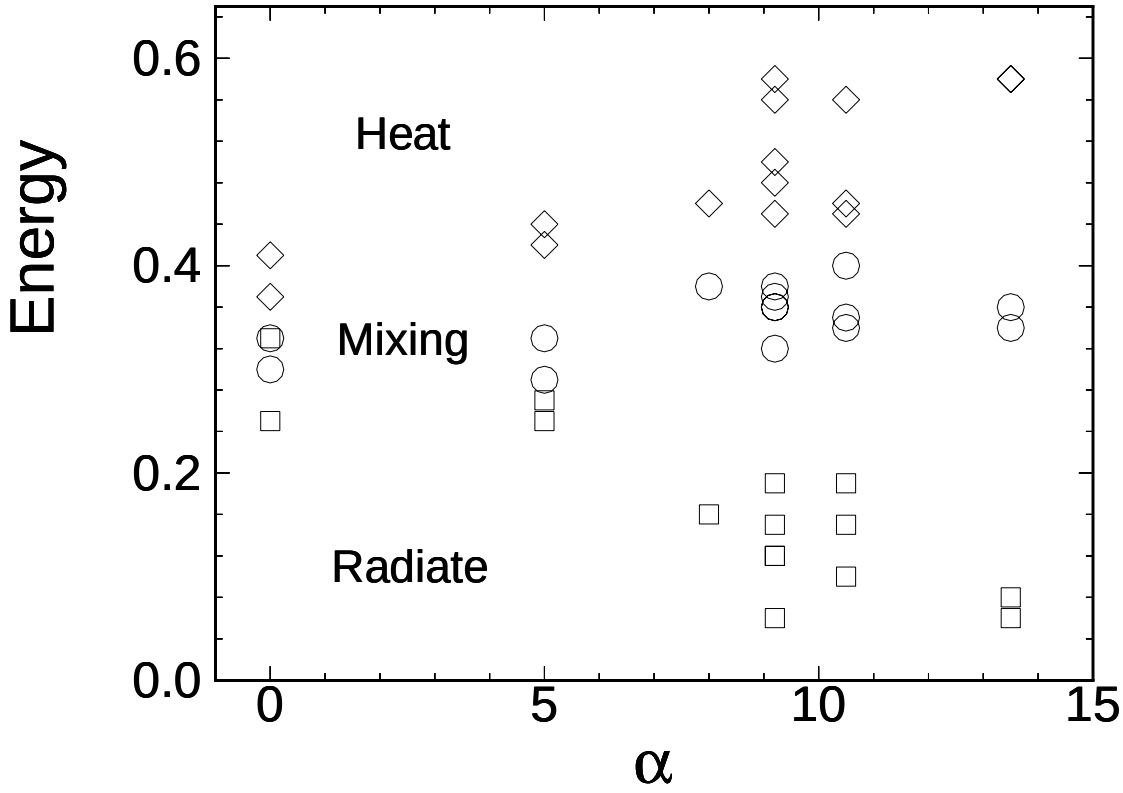

Figure 24: Values of mixing efficiency (circles), heat gain (diamonds), and energy radiated from the boundary layer region (squares) for simulations with bottom slopes between 0^o and 13.5^o.

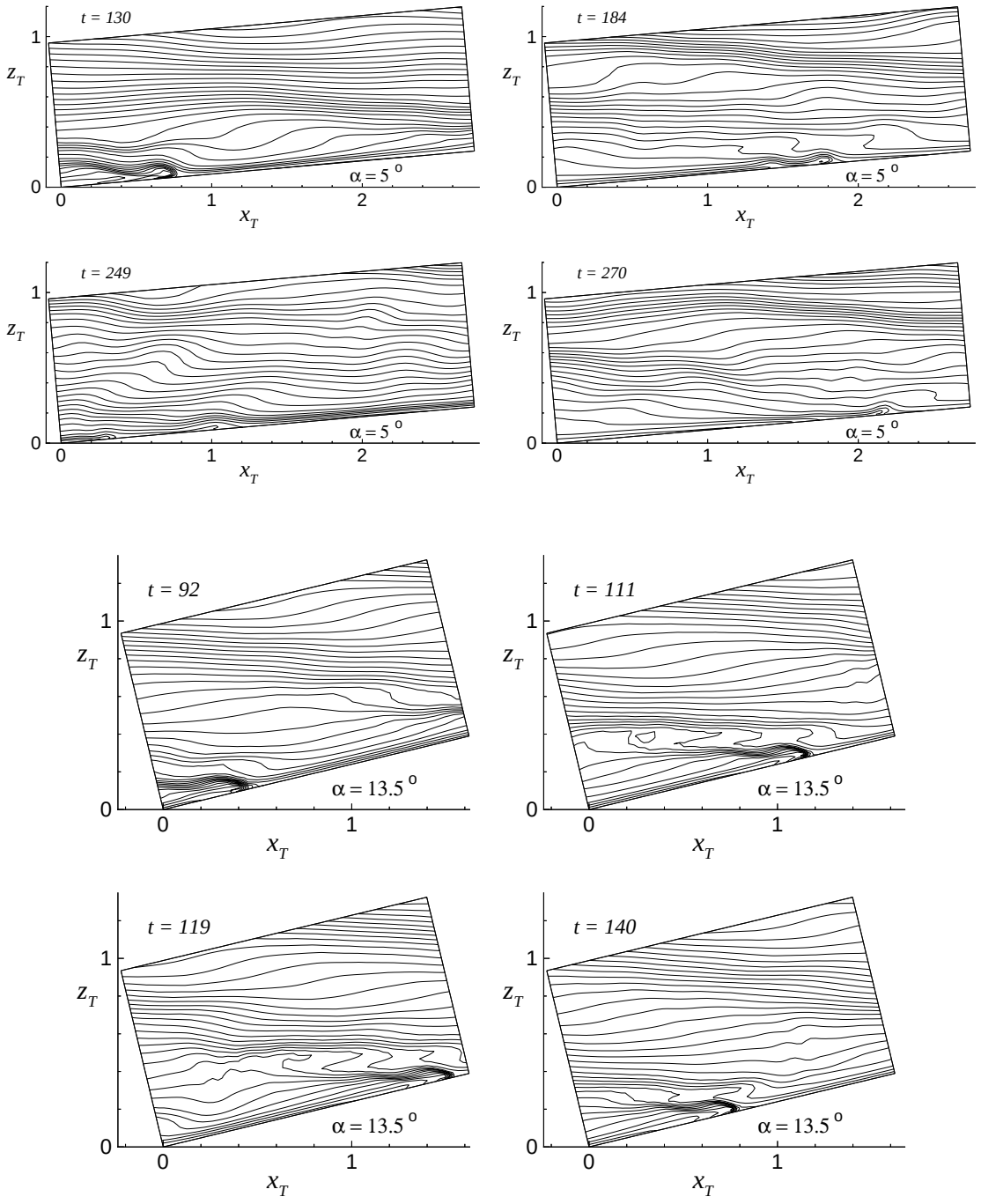

Figure 25: Isopycnals for internal wave reflection for subcritical and supercritical reflection, for Cases 38 and 50.